Comprehensive Representation of Tropical–Extratropical Teleconnections Obstructed by Tropical Pacific Convection Biases in CMIP6

XIAOFANG FENG,[a,b,c] QINGHUA DING,[b] LIGUANG WU,[a] CHARLES JONES,[b] HUIJUN WANG,[c,d] MITCHELL BUSHUK,[e] AND DÁNIEL TOPÁL[b,f,g]

[a] *Department of Atmospheric and Oceanic Sciences and Institute of Atmospheric Sciences, Fudan University, Shanghai, China*
[b] *Department of Geography, and Earth Research Institute, University of California, Santa Barbara, Santa Barbara, California*
[c] *Key Laboratory of Meteorological Disaster, Ministry of Education, Nanjing University of Information Science and Technology, Nanjing, China*
[d] *Collaborative Innovation Center on Forecast and Evaluation of Meteorological Disasters, Ministry of Education, Nanjing University of Information Science and Technology, Nanjing, China*
[e] *Geophysical Fluid Dynamics Laboratory, Princeton, New Jersey*
[f] *Institute for Geological and Geochemical Research, Research Centre for Astronomy and Earth Sciences, MTA-Centre of Excellence, ELKH, Budapest, Hungary*
[g] *Université Catholique de Louvain, Louvain-la-Neuve, Belgium*

(Manuscript received 12 July 2022, in final form 21 June 2023, accepted 1 July 2023)

ABSTRACT: The central role of tropical sea surface temperature (SST) variability in modulating Northern Hemisphere (NH) extratropical climate has long been known. However, the prevailing pathways of teleconnections in observations and the ability of climate models to replicate these observed linkages remain elusive. Here, we apply maximum covariance analysis between atmospheric circulation and tropical SST to reveal two coexisting tropical–extratropical teleconnections albeit with distinctive spatiotemporal characteristics. The first mode, resembling the Pacific–North American (PNA) pattern, favors a tropical–Arctic in-phase (warm Pacific–warm Arctic) teleconnection in boreal spring and winter. However, the second mode, with a slight seasonal preference of summer, is manifested as an elongated Rossby wave train emanating from the tropical eastern Pacific that features an out-of-phase relationship (cold Pacific–warm Arctic) between tropical central Pacific SSTs and temperature variability over the Arctic (referred to as the PARC mode). While climate models participating in phase 6 of the Coupled Model Intercomparison Project (CMIP6) appear to successfully simulate the PNA mode and its temporal characteristics, the majority of models' skill in reproducing the PARC mode is obstructed to some extent by biases in simulating low-frequency SST and rainfall variability over the tropical eastern Pacific and the climatological mean flow over the North Pacific during boreal summer. Considering the contribution of the PARC mode in shaping low-frequency climate variations over the past 42 years from the tropics to the Arctic, improving models' capability to capture the PARC mode is essential to reduce uncertainties associated with decadal prediction and climate change projection over the NH.

SIGNIFICANCE STATEMENT: This study focuses on the skill of models in phase 6 of the Coupled Model Intercomparison Project (CMIP6) in simulating two leading observed Northern Hemisphere (NH) teleconnections that show distinctive spatial and temporal characteristics. The first one, the Pacific–North American (PNA) mode, exhibits a warm Pacific–warm Arctic pattern in boreal spring and winter, and the second one, the Pacific–Arctic (PARC) mode, features a cold Pacific–warm Arctic out-of-phase relationship. We find that models are skillful in simulating the PNA mode but not the PARC mode. This limitation may be rooted in unrealistic simulations of the mean state of winds and the low-frequency sea surface temperature variability in the tropical eastern Pacific. These biases call for caution when interpreting current models' projections of extratropical circulations on multidecadal time scales.

KEYWORDS: Northern Hemisphere; Rossby waves; Teleconnections; Climate models; Clustering

1. Introduction

Tropical sea surface temperature (SST) variability modulates extratropical climate through the generation of recurrent modes of large-scale atmospheric circulation, the so-called teleconnection patterns (Wallace and Gutzler 1981; Barnston and Livezey 1987; Trenberth et al. 1998; Joseph and Srinivasan 1999).

Supplemental information related to this paper is available at the Journals Online website: https://doi.org/10.1175/JCLI-D-22-0523.s1.

Corresponding author: Qinghua Ding, qinghua@ucsb.edu

DOI: 10.1175/JCLI-D-22-0523.1

Previous studies highlight the Pacific–North American (PNA) pattern as the dominant Northern Hemisphere (NH) teleconnection that bridges SST variability associated with El Niño–Southern Oscillation (ENSO) with extratropical climate via stationary Rossby wave propagation on interannual time scales (Wallace and Gutzler 1981; Horel and Wallace 1981; Neelin et al. 1992; Trenberth et al. 1998; Wang et al. 2000). The PNA positive phase refers to positive SST anomalies in the tropical Pacific enhancing the midlatitude jet stream toward the western United States primarily in boreal winter.

In principle, the summertime extratropical circulation is less sensitive to tropical SST forcing than in winter, stemming from both the poleward displacement of jet streams associated with the weakened equator-to-pole thermal gradient and more active diabatic heating changes within the Asian summer monsoon region (Trenberth et al. 2014; Stan et al. 2017; Yuan et al. 2018; McCrystall et al. 2020; Henderson et al. 2021). Various summer teleconnections have been identified to be essential in modulating the Indian and East Asian summer monsoons, such as the Silk Road pattern (SRP) (Lu et al. 2002; Kosaka et al. 2009; Wang et al. 2017) and the Pacific–Japan (PJ) pattern (Wakabayashi and Kawamura 2004; Kosaka and Nakamura 2010; Choi et al. 2010). In particular, the most prominent teleconnection in the NH summer is the circumglobal teleconnection (CGT) exhibiting a zonal wavenumber-5 to wavenumber-7 structure along the midlatitudes that is connected to the Indian summer monsoon variability (Ding and Wang 2005; Ding et al. 2011; Wu et al. 2019).

More recent studies highlight the importance of the so-called Pacific–Arctic teleconnection (PARC) and associated tropical SST forcing in partially explaining the observed summertime warming in and around the Arctic (Ding et al. 2014; Trenberth et al. 2014; Perlwitz et al. 2015; Cohen 2016; Hu et al. 2016; Deser et al. 2017a; Vavrus 2018; Baxter et al. 2019; Feng et al. 2021), a mechanism that is underrepresented in Coupled Model Intercomparison Project phase 5 (CMIP5) multimodel and single-model large ensemble simulations (Topál et al. 2020). In contrast to the PNA, the PARC exhibits a longer-stretching Rossby wave train emanating from the tropics to the Arctic allowing for cold SST anomalies over the tropical east-central Pacific to remotely enhance Arctic warming near Greenland in its positive phase. Furthermore, the PARC is found to be a recurrent teleconnection on multidecadal and centennial time scales over the past two millennia in a 2000-yr-long proxy data constrained reanalysis (Feng et al. 2021).

Considering the essential role for tropical–extratropical atmospheric teleconnections in bridging the impacts of tropical SST forcing with the extratropics (Trenberth et al. 2014; Baggett and Lee 2015; Hoskins and Woollings 2015; Sigmond and Fyfe 2016), the reliability of climate models to replicate leading teleconnections in observations, such as the PNA, PARC, and other well-known modes, is of primary interest in this study. To elaborate on these issues, here we take a two-step approach. First, we use maximum covariance analysis (MCA) to objectively search for the leading modes of observed covariability between monthly NH atmospheric circulation and tropical SSTs. These modes represent the most prevalent forms of atmospheric circulation response in the extratropics to tropical SST forcing throughout the year. Second, we apply the MCA method on the same variables derived from Coupled Model Intercomparison Project phase 6 (CMIP6; Eyring et al. 2016) models to study how current climate models replicate the observed teleconnections as well as to further diagnose sources of possible model deficiencies (Stoner et al. 2009; Liu et al. 2017; Chen et al. 2018; Orbe et al. 2020). Through this evaluation, we expect to assess model biases in reproducing observed teleconnections in the NH with major implications for guiding future efforts aimed at improving decadal prediction.

2. Data and methods

a. *Reanalysis data and CMIP6*

We focus our analysis on the time period 1979–2020 using monthly (i) geopotential height and surface air temperature from the ERA5 reanalysis (Hersbach et al. 2020), (ii) global SST from the NOAA Extended Reconstructed Sea Surface Temperature version 5 (ERSSTv5) (Huang et al. 2017), (iii) sea ice extent from the National Snow and Ice Data Center (NSIDC) (Cavalieri et al. 1996; Fetterer and Knowles 2004), and (iv) global gridded precipitation data from the Global Precipitation Climatology Project (GPCP) (Adler et al. 2003). We also use monthly geopotential height and surface air temperature from the ERA Twentieth Century Reanalysis (ERA-20C) (Stickler et al. 2014) for 1900–2010. To evaluate models' performance in capturing the observed teleconnections, we focus on historical simulations (1979–2014) from 34 climate models archived in CMIP6 (Eyring et al. 2016). Detailed information on the 34 climate models is shown in Table 1.

b. *Maximum covariance analysis*

Maximum covariance analysis (MCA) (Bretherton et al. 1992; Wallace et al. 1992) is used to determine coupled variability between NH 200-hPa geopotential height (Z200) and tropical SST (30°S–30°N) via singular value decomposition of their covariance matrix. The leading modes contain time series and spatial patterns of the two fields that are optimally coupled. The squared covariance fraction (SCF) accounts for the percentage of total squared covariance in each mode, with the larger SCF indicating a higher dominance of the corresponding mode in accounting for the total covariance. In our study, we apply MCA on the two reanalysis datasets and 34 historical simulations of CMIP6, separately. To facilitate a direct comparison between MCAs derived from reanalyses and simulations, the horizontal resolutions of Z200 and SST fields from these datasets are interpolated onto a regular $2° \times 2°$ grid and the climatological annual cycle is removed from the monthly data at each grid point before applying MCA.

c. *Self-organizing map clustering method*

To objectively gauge multimodel performance with respect to their successes in replicating observed teleconnections, we primarily use the self-organizing map (SOM) method to perform a clustering analysis on spatial patterns of MCA modes derived from each model. This method is a type of artificial neural network algorithm that is trained using unsupervised

TABLE 1. The historical simulations from the first ensemble member runs of 34 CMIP6 models are used in this study.

No.	Model	Research center
1	ACCESS-CM2	Commonwealth Scientific and Industrial Research Organization (CSIRO) and Australian Research Council Centre of Excellence for Climate System Science (ARCCSS), Australia
2	ACCESS-ESM1-5	Commonwealth Scientific and Industrial Research Organization (CSIRO) and Australian Research Council Centre of Excellence for Climate System Science (ARCCSS), Australia
3	BCC-CSM2-MR	Beijing Climate Center, China Meteorological Administration, China
4	BCC-ESM1	Beijing Climate Center, China Meteorological Administration, China
5	CAMS-CSM1-0	Chinese Academy of Meteorological Sciences, China
6	CESM2	Community Earth System Model contributors, United States
7	CESM2-FV2	Community Earth System Model contributors, United States
8	CESM2-WACCM	Community Earth System Model contributors, United States
9	CESM2-WACCM-FV2	Community Earth System Model contributors, United States
10	CIESM	Tsinghua University–Department of Earth System Science (THU), China
11	CanESM5	Canadian Centre for Climate Modeling and Analysis, Canada
12	E3SM-1-0	Lawrence Livermore National Laboratory (LLNL), United States
13	E3SM-1-1	Lawrence Livermore National Laboratory (LLNL), United States
14	FGOALS-f3-L	LASG, Institute of Atmospheric Physics, Chinese Academy of Sciences, China
15	FGOALS-g3	LASG, Institute of Atmospheric Physics, Chinese Academy of Sciences, China
16	GFDL-ESM4	NOAA Geophysical Fluid Dynamics Laboratory, United States
17	GISS-E2-1-G	NASA Goddard Institute for Space Studies, United States
18	GISS-E2-1-G-CC	NASA Goddard Institute for Space Studies, United States
19	GISS-E2-1-H	NASA Goddard Institute for Space Studies, United States
20	INM-CM4-8	Institute for Numerical Mathematics, Russia
21	INM-CM5-0	Institute for Numerical Mathematics, Russia
22	IPSL-CM6A-LR	Institut Pierre Simon Laplace, France
23	KACE-1-0-G	National Institute of Meteorological Sciences–Korea Meteorology Administration, South Korea
24	MCM-UA-1-0	University of Arizona, United States
25	MIROC6	Atmosphere and Ocean Research Institute (The University of Tokyo), National Institute for Environmental Studies, and Japan Agency for Marine-Earth Science and Technology, Japan
26	MPI-ESM-1-2-HAM	Max Planck Institute for Meteorology, Germany
27	MPI-ESM1-2-LR	Max Planck Institute for Meteorology, Germany
28	MRI-ESM2-0	Meteorological Research Institute, Japan
29	NESM3	Nanjing University of Information Science and Technology, China
30	NorCPM1	NorESM Climate modeling Consortium, Norway
31	NorESM2-LM	NorESM Climate modeling Consortium, Norway
32	NorESM2-MM	NorESM Climate modeling Consortium, Norway
33	SAM0-UNICON	Seoul National University, South Korea
34	TaiESM1	Research Center for Environmental Changes (AS-RCEC), Taiwan

machine learning techniques to extract a few representative modes from input patterns (Kohonen 1990). This method has been extensively used to extract leading circulation modes over a specific region (e.g., Gibson et al. 2017) or analyze temporal dynamics of model errors in hydrological modeling (e.g., Herbst et al. 2009; Reusser et al. 2009), but applications on evaluating climate model performance remain limited.

Here, we use this method to group a set of leading MCA modes derived from CMIP6 models into a number of well-distinguished nodes. We also use conventional assessment metrics including pattern correlation and root-mean-square error (RMSE) to evaluate the leading MCA modes in CMIP6 against observed counterparts. Thus, these three methods (pattern correlation, RMSE, and SOM) collectively provide a comprehensive examination to better characterize and analyze multimodel performance in replicating the observed spatial and temporal characteristics of the teleconnections.

d. *Testing the significance of correlation coefficients*

To evaluate the statistical significance of the temporal correlation coefficient, the effective sample size N^* (Bretherton et al. 1999) is used according to the following equation:

$$N^* = N\frac{1 - r_1 r_2}{1 + r_1 r_2}, \tag{2.1}$$

where N is the number of available time steps and r_1 and r_2 are lag-one autocorrelation coefficients of each variable. A confidence level above 95% is used to determine the significance of correlations throughout the study.

e. *The Rossby wave source, stationary Rossby wavenumber, and wave activity flux*

To understand how atmospheric dynamics driven by tropical SST contribute to the establishment of extratropical teleconnections in the form of stationary Rossby waves, based on the

derivation of the nonlinear vorticity equation (Sardeshmukh and Hoskins 1988), the so-called Rossby wave source (RWS) at a specific pressure level can be calculated as

$$\mathrm{RWS} = -\nabla \cdot (V_\chi \zeta), \tag{2.2}$$

where ζ is absolute vorticity calculated as the sum of relative vorticity and planetary vorticity, and V_χ is the divergent component of the total wind V at the same vertical level.

In addition, based on an idealized theoretical model (Hoskins and Ambrizzi 1993), the stationary Rossby wavenumber (K_s) of the basic flow in the upper troposphere is calculated to estimate what types of stationary Rossby wave trains are preferentially supported by the mean flow in the extratropics. The K_s is calculated as

$$K_s = \left(\frac{\beta_*}{\overline{U}}\right)^{1/2}, \tag{2.3}$$

where $\overline{U}$ is the westerly mean flow (positive), with

$$\beta_* = \beta - \frac{\partial^2 \overline{U}}{\partial y^2}, \tag{2.4}$$

where β is the meridional gradient of the Coriolis parameter.

Wave activity flux, in the form of Eq. (2.5) derived in Plumb (1985), is calculated to illustrate how the group velocity associated with a Rossby wave train horizontally propagates along the path. The flux F_s takes the form

$$F_s = p\cos\phi \left\{ \begin{array}{l} \dfrac{1}{2a^2\cos^2\phi}\left[\left(\dfrac{\partial\psi'}{\partial\lambda}\right)^2 - \psi'\dfrac{\partial^2\psi'}{\partial\lambda^2}\right] \\ \dfrac{1}{2a^2\cos\phi}\left(\dfrac{\partial\psi'}{\partial\lambda}\dfrac{\partial\psi'}{\partial\phi} - \psi'\dfrac{\partial^2\psi'}{\partial\lambda\partial\phi}\right) \end{array} \right\}, \tag{2.5}$$

where the streamfunction $\psi = \Phi/2\Omega\sin\phi$, where Φ is the geopotential and Ω is Earth's rotation rate, a is Earth's radius, p = pressure/1000 hPa, and (ϕ, λ) are latitude and longitude respectively.

3. Two leading teleconnection modes in the NH and their seasonality in observations

a. *Two leading NH teleconnections identified by MCA*

To explore leading modes of the NH atmospheric circulation variability associated with tropical SSTs, while excluding the imprints of global warming as approximated by secular trends in the two fields, we perform MCA between detrended monthly Z200 in the NH and tropical SST (30°S–30°N) for the period 1979–2020. The first two MCA modes together explain 86.4% (76.9% and 9.5%, respectively) of the total squared covariance between the two variables. The first MCA mode (MCA1) of Z200 and related wave activity flux [Eq. (2.5)] shows a hemispheric teleconnection propagating from the tropical Pacific to the midlatitudes with a high pressure in the tropics and western North America in its positive phase, concomitant to warm tropical SST anomalies over the eastern Pacific (Figs. 1a,c). This leading MCA mode resembles the well-known PNA pattern (e.g., Wallace and Gutzler 1981) that links the forcing of ENSO to circulation anomalies over the North Pacific and North America, hereafter referred to as the PNA mode. The time series associated with the PNA mode is characterized by remarkable interannual variability, with peaks indicating strong El Niño events in 1982/83, 1997/98, 2009/10, and 2014–16 and strong La Niña events in 1988/89, 1998–2001, and 2010–12 (Fig. 1e).

The second MCA mode (MCA2) of Z200 yields a different type of teleconnection pattern favoring a Rossby wave train emanating from the tropical eastern Pacific to the Arctic with low pressure over the tropical central Pacific and high pressure over Greenland (Fig. 1b). It is accompanied by a zonally uniform height rise along the NH midlatitudes with successive isolated high pressure centers in its positive phase. The wave activity flux related to this pattern shows clear energy transport from the tropics to the Arctic along its path (Fig. 1b). This MCA mode is consistent with a tropical–Arctic teleconnection pattern, known to be partially responsible for Arctic surface warming and sea ice melting in the past two decades (Ding et al. 2014; Trenberth et al. 2014; Hu et al. 2016; Baxter et al. 2019; Jeong et al. 2022; Fig. 2b), and associated with cold tropical SST anomalies extending from the equatorial central Pacific to the Gulf of California (Fig. 1d), hereafter referred to as the Pacific–Arctic (PARC) mode. This SST pattern bears some resemblance to the negative phase of the PDO over the tropical Pacific and the corresponding MCA2 time series indicates that its temporal variability may possess some elements oscillating on decadal time scales. Furthermore, the resemblance of the Z200 and SST spatial patterns associated with the PARC mode, derived from detrended monthly data, to the linear trends of monthly Z200 and SST during 1979–2020 is noticeable. Both show a wavy structure in the NH midlatitudes and the absence of tropical SST warming in the east-central Pacific (Fig. 2a). This suggests that the PARC mode may partially explain the spatial structure of observed changes over the past 42 years in tropical SST and NH circulation, which implies a recent strengthening of the PARC (Ding et al. 2014; Feng et al. 2021). In addition, the PARC mode serves as MCA2 with a larger squared covariance (21.7%, and 48.6% for MCA1) if the MCA calculation focuses on the connection between tropical SST and NH extratropical Z200 (30°–90°N) (see Fig. 1 in the online supplemental material).

Although both the PNA and PARC teleconnection modes are sensitive to tropical SST over the eastern Pacific, their SST patterns and temporal characteristics are different. It is informative to further investigate their seasonality to better understand the seasonal dependence of each mode. To do so, we calculate the squared expansion coefficient (SEC) index by squaring the values of the normalized MCA time series and averaging them for each month (Figs. 2c,d). This allows us to investigate the dominance of each mode in terms of explained covariance throughout the year. Our calculations imply that both the Z200 patterns of the PNA and the PARC possess the strongest action in winter and spring, while the SST mode associated with the PARC turns out to be more active in summer and also has a weaker seasonal preference than the PNA (Wallace and Gutzler 1981; Ding et al. 2011; Baxter et al. 2019; Figs. 2c,d). The manner in which the PNA and the PARC modes interact with each other throughout the year may

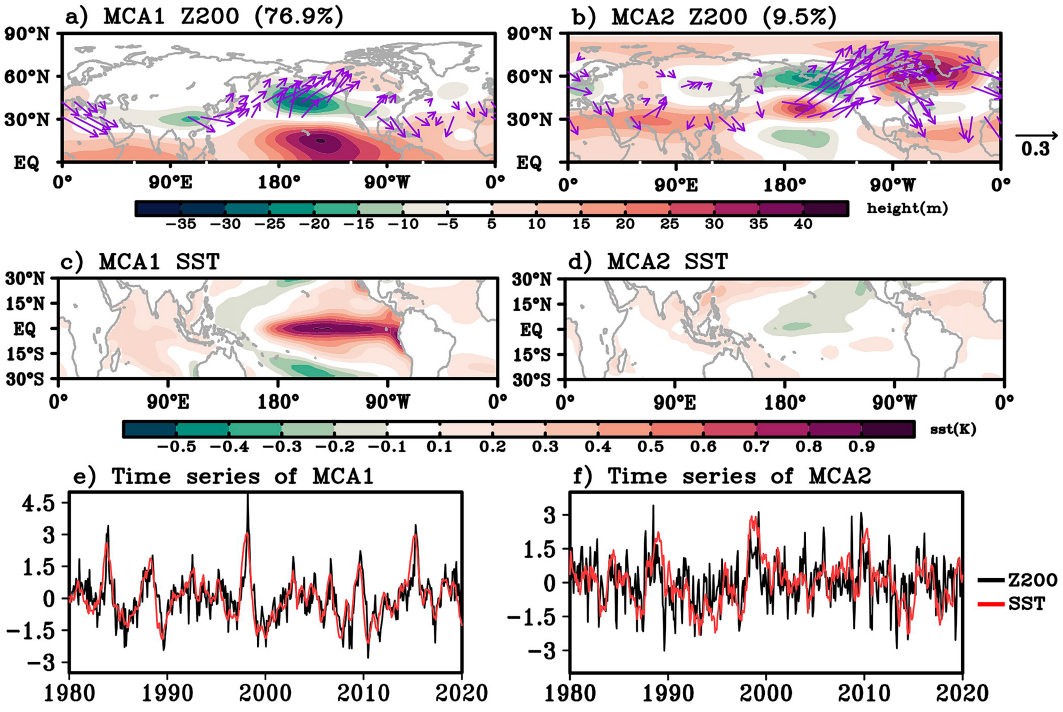

FIG. 1. Two leading NH teleconnection modes during 1979–2020 in ERA5. The first mode of MCA (MCA1) between detrended monthly mean (a) 200-hPa geopotential height (Z200; m) and (c) tropical sea surface temperature (SST; °C) with (e) normalized time series associated with MCA1 Z200 (black curves) and SST (red curves) patterns shown in (a) and (c). (b),(d),(f) As in (a), (c), and (e), but for the second MCA mode (MCA2). The squared covariance fraction (SCF; %) explained by each MCA mode is indicated in the title of each panel in (a) and (b). In (a) and (b), purple vectors ($\times 10^4$ Pa m^2 s^{-2}; vectors less than 10^4 Pa m^2 s^{-2} are omitted) denote the wave activity flux [Eq. (2.5)] associated with the corresponding MCA Z200 pattern. The correlation coefficient between the time series of MCA1 Z200 and SST is 0.77 in (e) and 0.52 for MCA2 in (f).

be regulated by ENSO-related SST variability, which normally peaks in winter over the eastern Pacific and becomes much weaker in summer. This allows other SST modes such as the interdecadal Pacific oscillation (IPO) or the Pacific meridional mode (PMM; Chiang and Vimont 2004) to excite extratropical circulation responses from the tropical eastern Pacific in boreal summer.

b. *Impacts of the PNA and PARC on extratropical climate*

To further elaborate on the implications of the recent strengthening of the PARC and how the PNA and PARC impact extratropical climate, we calculate the correlation between surface temperature and the time series of the first two MCA Z200 modes in each month and season. As for the PNA, it primarily reflects associated surface temperature changes in the tropics and in the North Pacific with warming in the northwestern United States and Alaska, especially in winter (Figs. 3a–e). In contrast, NH surface temperature changes sensitive to the PARC mode exhibit a distinctive spatial pattern, which mirrors the structure of the MCA2 Z200 mode: concomitant to a tilted cold SST anomaly extending from the equatorial central Pacific to the Gulf of California, and vast warming over some continental regions particularly around Greenland, eastern North America, and northern Eurasia in summer (Fig. 3h). Atmospheric circulation associated with the PARC mode also significantly correlates negatively with Eurasian/Siberian temperatures in winter and spring (Figs. 3g,j), which indicates that tropical SST variability may partially modulate the Eurasian cooling observed in recent decades through the PARC teleconnection (Mori et al. 2014; Matsumura and Kosaka 2019; Feng et al. 2021). This PARC mode can explain almost 30% (squared coefficient) of surface temperature variability over Greenland in spring and summer and over midlatitude Eurasia in winter and spring. In addition, Arctic sea ice melting around the Beaufort Sea is closely connected to the PARC mode in the melting season (Fig. 2b). Consequently, the strengthening of this mode in summer and autumn can contribute to sea ice melting and related positive feedbacks in the Arctic on interannual time scales. More studies on the impact of the seasonality of the PARC are desired in order to fully understand the tropical–extratropical teleconnections, since extratropical circulation response to tropical diabatic heating is sensitive to changes in the climatological background flow (e.g., Lin et al. 2009; Seo and Son 2012).

c. *The PNA and PARC over the past 111 years*

Next, we show evidence for the existence and stability of these two teleconnections over longer periods before 1979. We

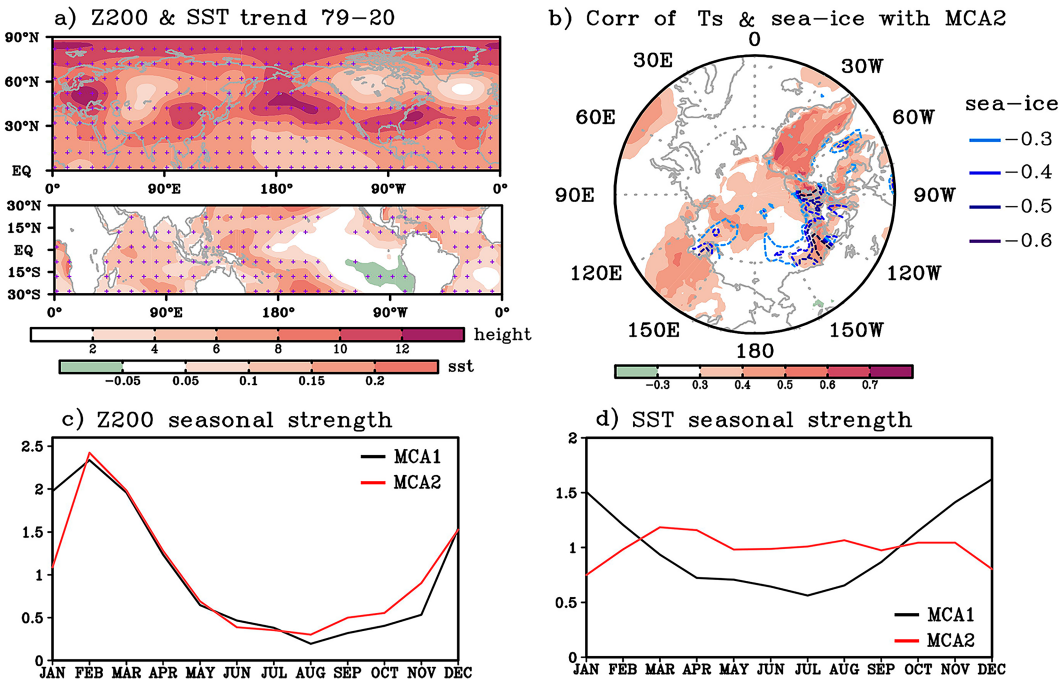

FIG. 2. Linear trends of monthly mean (a) Z200 (m decade^{-1}) and tropical SST (°C decade^{-1}) in 1979–2020. (b) Simultaneous correlations between time series of MCA2 Z200 and detrended surface temperature (Ts) in summer [June–August (JJA); shading] and sea ice extent in the melting season [June–October (JJASO); contours] displayed in polar projection. Squared expansion coefficient (SEC) indices of (c) MCA Z200 and (d) SST patterns by squaring the values of the normalized MCA1 (black curves) and MCA2 (red curves) time series and averaging them for each month. In (a), small crosses denote grid points with trends that are statistically significant at the 95% confidence level. In (b), grid points with statistically significant correlations above the 95% confidence level are displayed.

examine the two leading MCA modes of monthly Z200 and tropical SST from ERA-20C in 1900–2010. To reduce impacts of global warming over the twentieth century, we remove the linear trends of Z200 and SST before the analysis. The first two MCA modes' spatial patterns are in accordance with results seen using the ERA5 reanalysis: MCA1 (explaining 83.4% of SCF) closely resembles the PNA mode, and the MCA2 (explaining 9.0% of SCF) is similar to the PARC mode albeit an eastward extension of cold SST anomalies in the tropical eastern Pacific (although the tilted cold SST pattern differs slightly from its 42-yr counterpart), and a slight shift in the wavy pattern around the Arctic is seen compared with the pattern in ERA5 (Figs. 4a–d). The time series associated with MCA2 exhibits clear decadal to multidecadal oscillations throughout the whole period and a significant upward trend since 1979 (Fig. 4f), which suggests that low-frequency tropical SST variability captured by this mode plays a key role in modulating extratropical climate via the PARC-like teleconnection over the past 111 years. In particular, this mode's distinctive spatial pattern likely had an imprint on the long-term trends of NH circulation and tropical SST over the past 42 years. However, we cannot rule out the possibility that some of this low-frequency variability may also be due to aerosol-driven midcentury cooling (Shen et al. 2020).

Both the PNA and PARC modes appear to be the two leading teleconnections persistently over the past century, and thus are key agents to translate tropical forcing to the extratropics. These robust observed patterns can be used as a test bed to gauge models' skill in replicating the same linkage in simulations. Note that the third- and higher-order MCA modes of Z200 and tropical SST fields are not considered in this study, since the SCFs of these modes are well below 3% in ERA5 and 2% in ERA-20C during the past 42 and 111 years respectively.

4. CMIP6 models' performance in simulating the two teleconnection modes

To assess how CMIP6 models replicate the observed PNA and PARC modes, we perform MCA using monthly tropical SST and Z200 over the period 1979–2014 from each historical simulation in CMIP6. Consistent with the method applied to reanalyses, to focus on year-to-year variability and to reduce the influence of anthropogenic forcing, we remove the linear trends from the two variables before applying MCA. The first two MCA modes explain the majority of the total squared covariance in each CMIP6 model; however, it ranges from 46.5% to 96.6% for MCA1 and 1.28% to 14.9% for MCA2 (Fig. 5a) compared with the 76.9% for MCA1 and 9.5% for MCA2 in ERA5. All models successfully reproduce the key features of the PNA mode, while the spatial patterns of MCA2 vary substantially from model to model. To understand the overall skill of all models, we average the MCA spatial

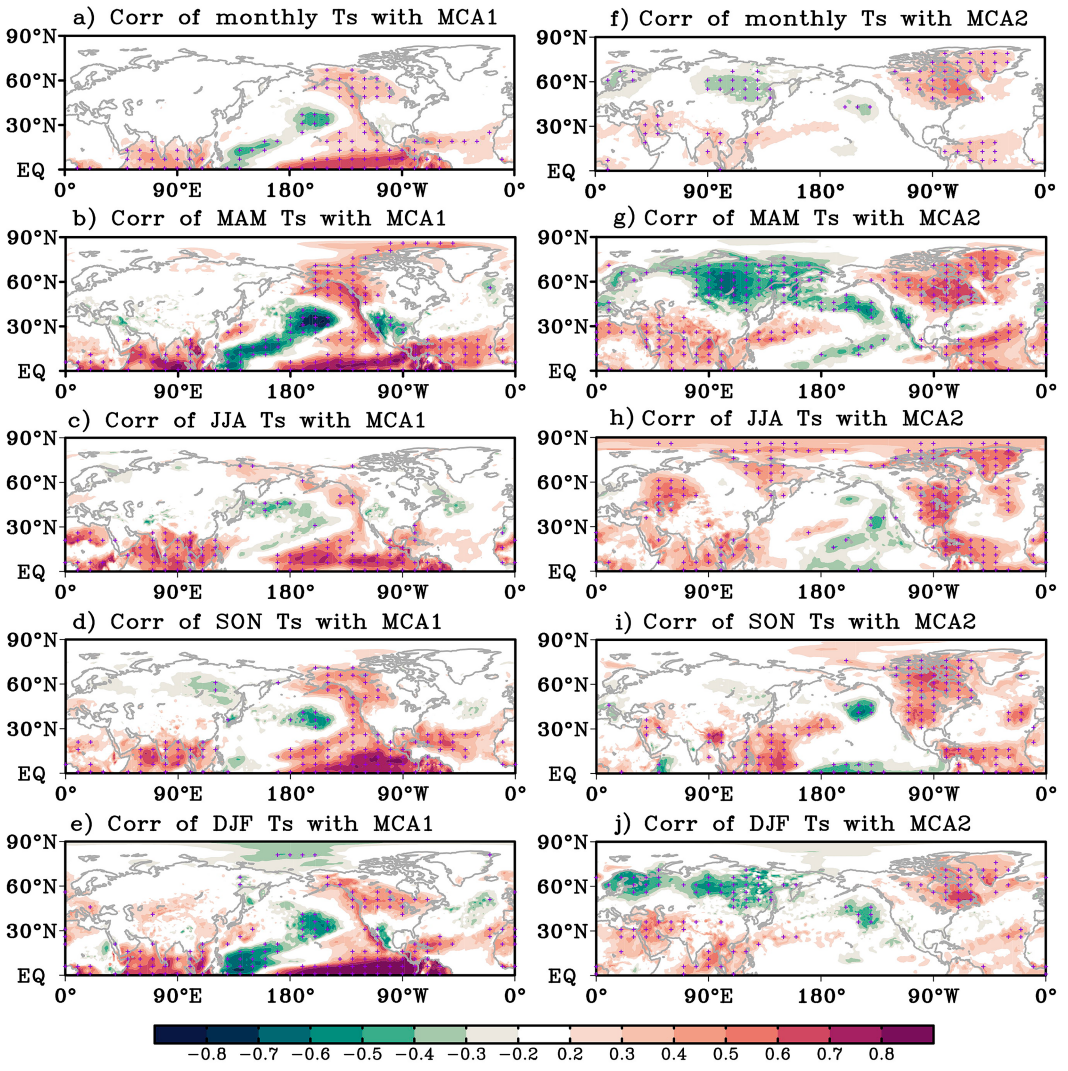

FIG. 3. Correlations between time series of MCA1 Z200 and detrended (a) monthly mean Ts and seasonal mean Ts in (b) MAM (March–May), (c) JJA (June–August), (d) SON (September–November), and (e) DJF (December–February, i.e., December of the previous year and January and February of the current year). (f)–(j) As in (a)–(e), but for MCA2. Stippling indicates statistically significant correlations at the 95% confidence level. To calculate the correlations for seasonal mean data, monthly Ts data and the time series of MCA1/MCA2 Z200 are averaged over each season respectively and then are correlated.

patterns of Z200 and SST across all models and each of the two modes and highlight those areas where 70% of the models agree on the simulated characteristics of the observed teleconnections (Figs. 5b–e), hereafter referred to as the ensemble mean MCA modes. In the ensemble mean MCA1, the tropical upper-level circulation displays a robust PNA-like response in the tropics and midlatitudes to anomalous warm tropical SSTs associated with El Niño, showing high pressure centers over the equatorial Pacific and western North America (Figs. 5b,d). It is also noted that the high-latitude component of the simulated PNA extends broadly into the Arctic, which is not seen in the observed MCA1 over the past 42 years (Figs. 1a,c).

The PARC mode is underestimated by many models, which is reflected in their ensemble mean (Figs. 5c,e). It is only over central locations of particular cells of the PARC (e.g., Greenland and the tropical eastern Pacific) where models show skill to capture part of the signals, also with smaller SCFs (~6.8% on average) compared with that in ERA5 (9.5%). We also calculate the squared expansion coefficient (SEC) index (as for ERA5 in Figs. 2c,d) for both modes grouped by months for each model, then we average the SEC indices across the models. The ensemble mean SEC indices show similar features to their observed counterparts (Figs. 2d and 5g).

To evaluate model performance regarding the simulation of spatial characteristics of the two modes, we consider the pattern correlation (r) and the root-mean-square error (RMSE). Pattern correlation coefficients of Z200 and SST MCA1 calculated for each model against ERA5 exhibit significant positive values

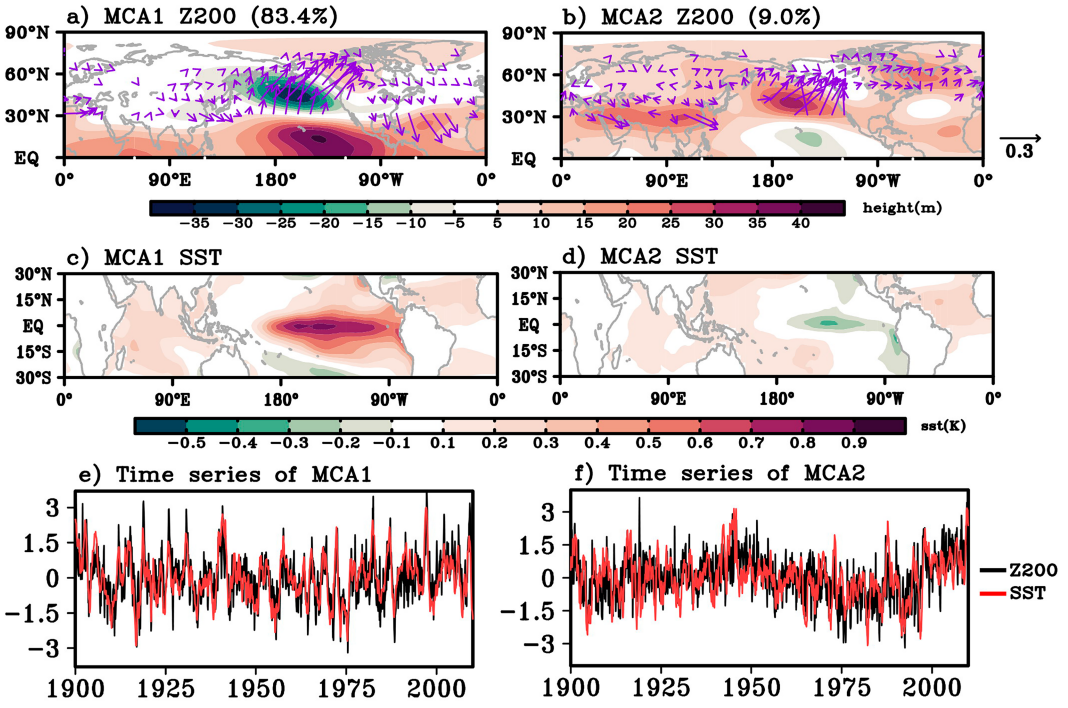

FIG. 4. The two leading NH teleconnection modes in the past 111 years in ERA-20C. The MCA1 between detrended (a) Z200 (m) and (c) tropical SST (°C) during the period 1900–2010 with (e) the normalized time series of MCA1 Z200 (black curves) and SST (red curves) shown in (a) and (c). (b),(d),(f) As in (a), (c), and (e), but for MCA2. In (a) and (b), purple vectors ($\times 10^4$ Pa m^2 s^{-2}; vectors less than 10^4 Pa m^2 s^{-2} are omitted) denote the wave activity flux [Eq. (2.5)] associated with the corresponding MCA Z200 pattern. The SCF explained by each MCA mode is indicated in the title of each panel in (a) and (b). The correlation coefficient between the time series of MCA1 Z200 and SST is 0.72 in (e) and 0.54 for MCA2 in (f).

in all models (r_{Z200} = 0.84 and r_{SST} = 0.81 on average), as well as small RMSE (RMSE$_{Z200}$ = 7.79 and RMSE$_{SST}$ = 0.18 on average), indicative of a well-represented PNA mode in CMIP6 models (Figs. 6a,b). In contrast, pattern correlation coefficients of Z200 and SST MCA2 for each model against ERA5 vary from −0.3 to 0.8 (r_{Z200} = 0.30 and r_{SST} = 0.35 on average) with much larger RMSE in the Z200 field (RMSE$_{Z200}$ = 15.37 and RMSE$_{SST}$ = 0.17 on average) compared with MCA1. Consistent with our previous comparison of the observed and simulated MCA modes using the multimodel ensemble means, these results suggest that models are able to successfully capture the PNA but not the PARC.

To further explore how each model simulates regional features of the two MCA modes, we use the SOM clustering method to classify MCA Z200 and SST modes derived from 34 models. This provides us a new opportunity to visualize how close models' simulations are to their observed counterparts spatially. The 34 MCA modes are grouped into a set of nodes based on similarities between their spatial patterns. A sole spatial pattern is generated to represent common spatial features of all members in each node. Then, the spatial correlation between each original pattern with its assigned node pattern is calculated and the total of 34 spatial correlation coefficients are considered to quantify the level of the success of the clustering. The appropriate node size should be selected to fully encompass key characteristics of simulated patterns derived from a limited sample size of 34 and also maximize the discrepancies between each node. The larger the node number is, the higher the coefficient and the more comprehensively models' features can be reflected in this clustering. By reducing the node number from 34 to a smaller node number, the averaged spatial correlation drops correspondingly to reflect the leading spatial features contained in original patterns. Considering the largest rate of the coefficient growth with increasing node numbers (Kohonen 1990), the first and second MCA modes are clustered into nine and six nodes with each reflecting 60% and 65% of the total spatial features, separately.

The 34 pairs of MCA1 are classified into nine groups that all well reflect the PNA mode with some slight differences around the Indian Ocean and southern Asia along 30°N, and the high latitudes in each group (Fig. 7). Pattern correlation coefficients of each group with the PNA mode in observations are approximately $r \sim 0.90$ and 0.95 for the Z200 and SST fields, respectively (Fig. 6c). In contrast, the MCA2 spatial patterns grouped into six nodes yield more diverse spatial structures, since the second mode is less consistent within the models (Fig. 8). The pattern correlation coefficients of Z200 and SST fields with the PARC mode in observations vary from r = 0.15 to 0.85 across the models (Fig. 6d). Most models tend to exhibit a strong zonally elongated height rise along the jet stream and

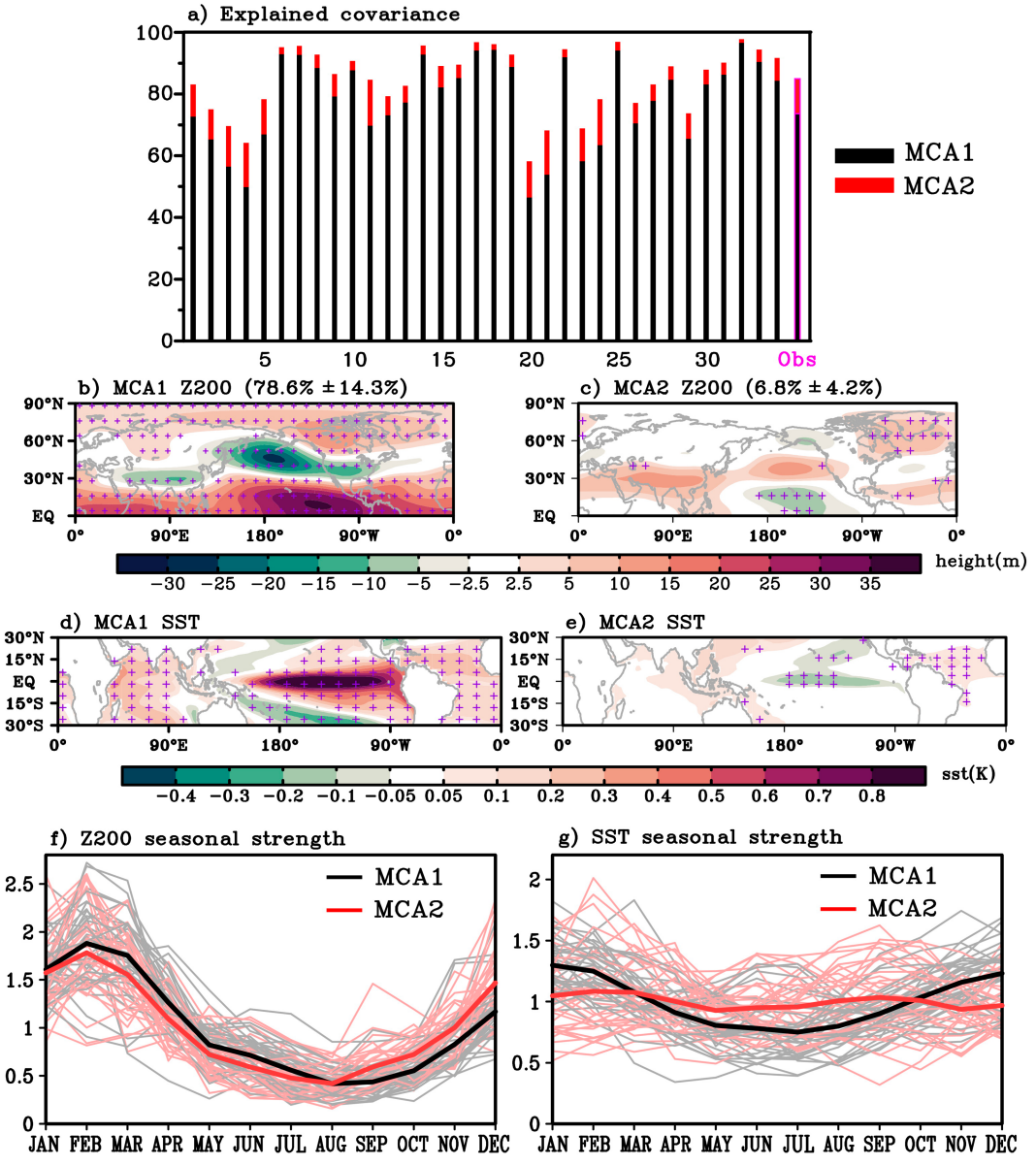

FIG. 5. CMIP6 model performance in reproducing the two leading NH teleconnection modes. (a) The SCF explained by MCA1 (black columns) and MCA2 (red columns) between detrended Z200 and tropical SST in the CMIP6 34 models. The multimodel ensemble means of MCA1 (b) Z200 (m) and (d) SST (°C) in the period 1979–2014. (c),(e) As in (b) and (d), but for MCA2. The ensemble means of squared coefficients of the time series associated with MCA1 (thick black curves) and MCA2 (thick red curves) for (f) Z200 and (g) SST patterns averaged in each month from the CMIP6 models. The SCF explained by MCA1 or MCA2 simulated by all the CMIP6 models (ensemble mean SCF ± the one standard deviation of SCFs across all models) is indicated in the title of each panel in (b) and (c). In (b)–(e), stippling indicates grids where a majority of (more than 70%) of the 34 models exhibit the same sign as that of the corresponding MCA pattern in observations (Figs. 1a–d). In (f) and (g), the light color curves indicate squared coefficients of the time series associated with MCA1 (light black curves) and MCA2 (light red curves) for the Z200 and SST patterns averaged in each month from each model.

show a PNA-like pattern over North Pacific (Figs. 8b–d, nodes 1–3, including 22 models). Some models primarily reflect variability in the middle and high latitudes revealing three main action centers located in the Arctic, North Pacific, and eastern North America (Figs. 8f,g, nodes 5–6, including 11 models). Only one model (Fig. 8e, node 4: CIESM) bears a strong resemblance to the PARC mode, albeit with weaker signals than the observed (pattern correlations: $r_{Z200} = 0.79$, $r_{SST} = 0.86$). Consistent with the other two evaluation methods (Figs. 6a,b), the SOM method reinforces that most CMIP6 models have some

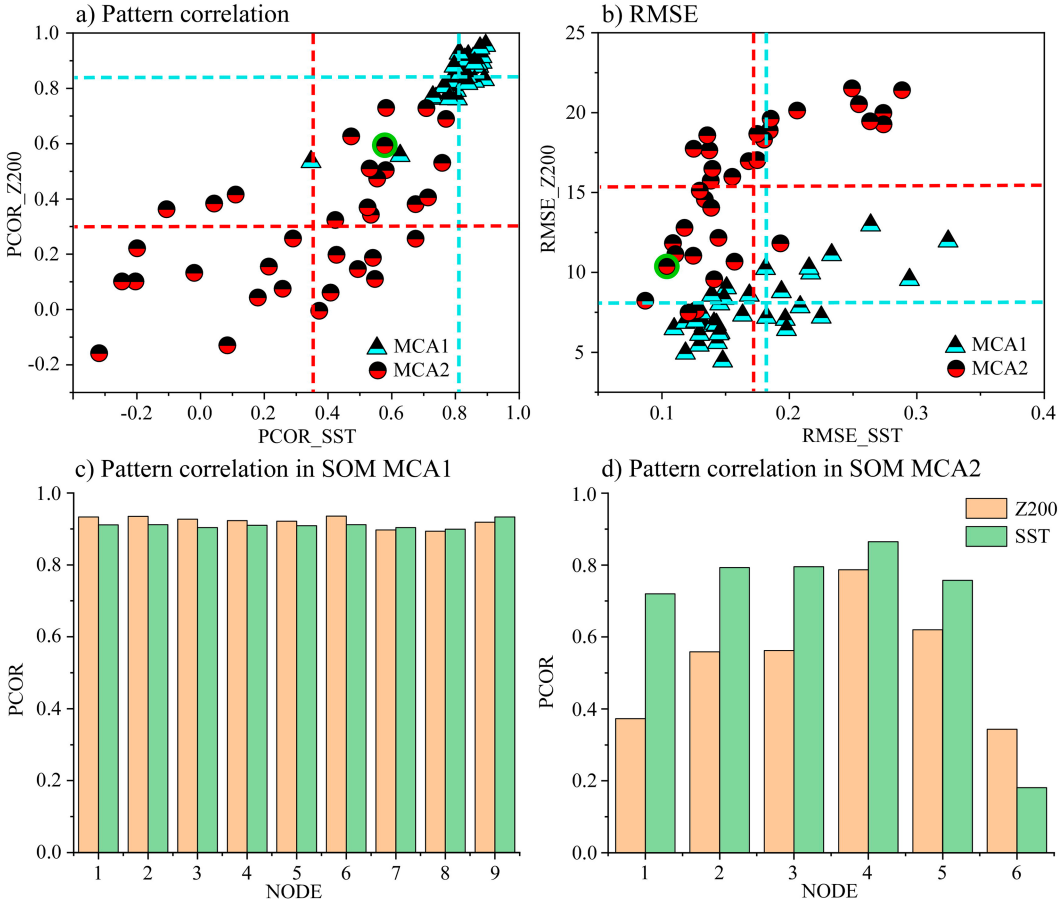

FIG. 6. Three methods are used to evaluate how CMIP6 models replicate the two leading NH teleconnection modes. (a) Pattern correlations and (b) root-mean-square error (RMSE) between the MCA1/2 (green triangles, red circles) Z200 or SST pattern derived from the CMIP6 models and the corresponding one in observations. Pattern correlations between the SOM-clustered (c) MCA1 and (d) MCA2 in each node and that of ERA5 in Figs. 1a–d. In (a) and (b), light green circles indicate the model (i.e., CIESM) in node 4 that is indicated to best resemble the PARC mode in the following SOM analysis (Fig. 8e). Dashed lines in (a) and (b) indicate the multimodel ensemble means of the pattern correlations and RMSE of MCA1 (blue lines) and MCA2 (red lines).

limitations in reproducing the PARC mode while they can successfully simulate the PNA.

5. Possible causes of model limitations in capturing the PARC mode

a. Limitations in simulating tropical SST and convection associated with the PARC

Why are models able to replicate the overall structure of the PNA mode while showing limitations in reproducing the PARC mode? Considering that ENSO is the leading driver of tropical SST variability and its extratropical forcing is deemed to be strong enough to overwhelm background climate noise in the midlatitudes, it is expected that most models have better skill at capturing the PNA than the PARC. Based on this line of thought, we further speculate that this limitation might stem from two possible causes. The first possible cause, explored in this subsection, is that the low model skill in capturing the PARC teleconnection is associated with a poor simulation of tropical SST variability on low-frequency time scales in the tropical eastern Pacific. The second possible cause, explored in the following subsection, is associated with errors in simulating the climatological summer circulation in the NH.

Over the past decades, substantial scientific progress has been made to improve simulation skills of ENSO, which likely results in a better simulation of the PNA, especially in winter when ENSO events peak in strength. However, the tropical SST variability associated with the PARC mode in observations and models is not the leading mode in the region, resembling the IPO or the PMM owing to strong linkages with extratropical oceanic processes (Chiang and Vimont 2004; Feng et al. 2021). In contrast to ENSO, these high-order SST modes have relatively weak magnitudes and more complex temporal variability and are subject to complex interactions with tropical–extratropical atmospheric and oceanic processes,

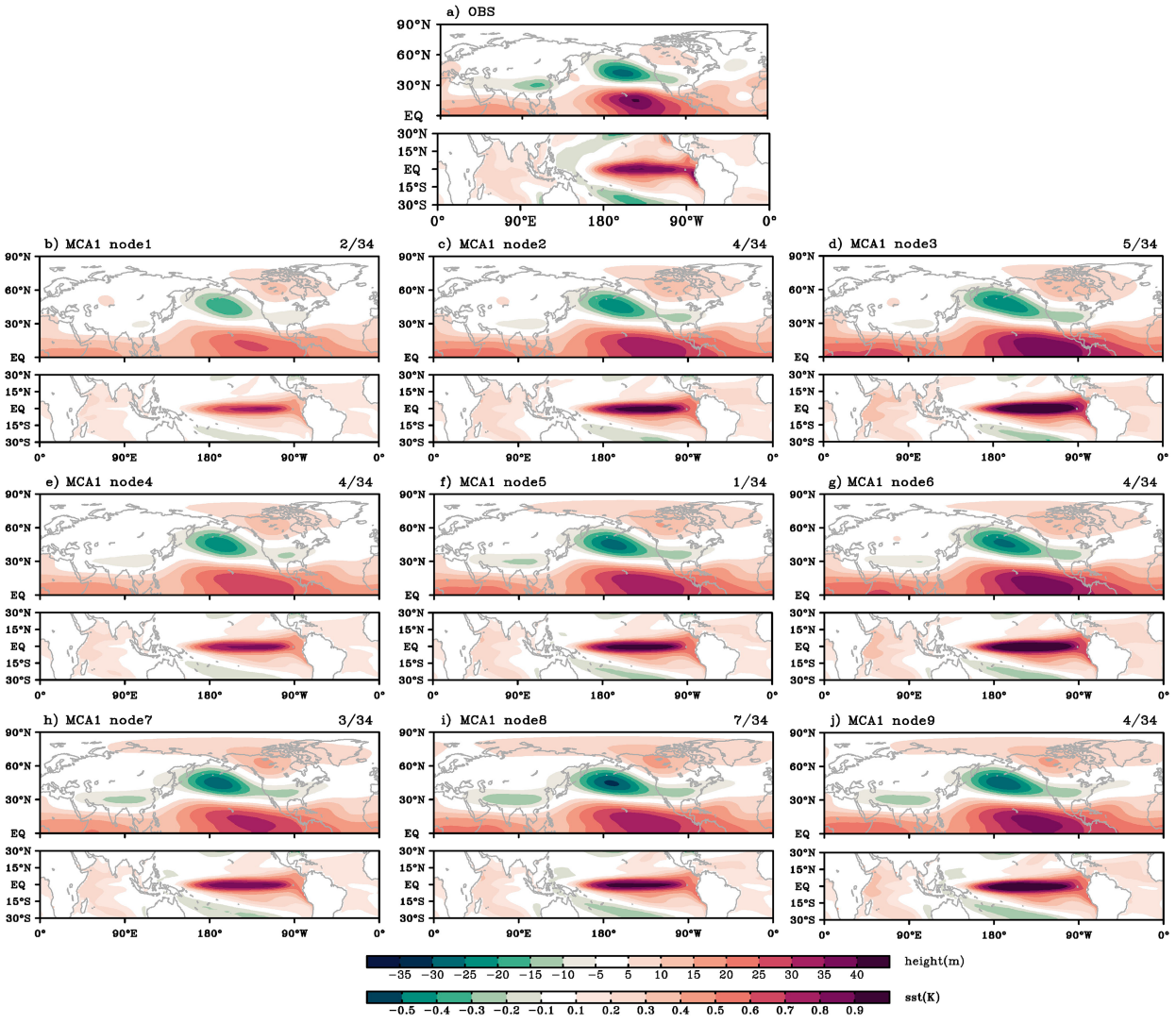

FIG. 7. Classifying simulated MCA1 by CMIP6 models using the SOM method. (a) MCA1 between detrended monthly mean Z200 (m) and tropical SST (°C) in observations, and (b)–(j) 34 MCA1 from the CMIP6 models clustered into nine nodes. The number of models grouped into each node is indicated in the title of each panel.

such as nonlinear oceanic dynamics (Sun et al. 2014; Lewis and Legrande 2015), momentum flux (Larson et al. 2018), and ocean heat content changes (Karnauskas et al. 2012). Thus, current climate models may still struggle to fully capture their underlying formation mechanisms (Deser et al. 2012a,b; Fasullo et al. 2020), which can obstruct the generation and maintenance of the PARC mode.

The biases in simulating these SST variations in the tropical eastern Pacific can further worsen the models' skill to simulate tropical convection and the RWS that is essential to generate the PARC. To address this issue, we examine boreal summer precipitation related to the PNA and PARC modes by regressing the observed and simulated precipitations onto the corresponding MCA1/2 SST time series, respectively. In line with our previous analyses, the multimodel ensemble means of PNA-mode regressed precipitation (averaged from the 34 models' regression maps) well reflect the observed rainfall anomalies over the tropical Pacific that are characterized by positive precipitation anomalies along the intertropical convergence zone (ITCZ; Figs. 9a,c). However, as for the PARC mode, the regression map of the multimodel ensemble mean reveals that models tend to underestimate precipitation anomalies in the deep tropics especially in the central-east Pacific compared with observations (Figs. 9b,d). Such biases in simulating tropical SST and convection variability can be translated to the generation of the RWS. The positive RWS over the central-east Pacific can support Rossby wave propagation from the tropics to midlatitudes in observations (see supplemental Fig. 2a). However, models behave differently in simulating RWS over tropical Pacific related to this mode. The multimodel ensemble means of the RWS exhibit weaker signals in the tropical eastern Pacific along 15°N compared with observations (supplemental Fig. 2b), although some models can capture

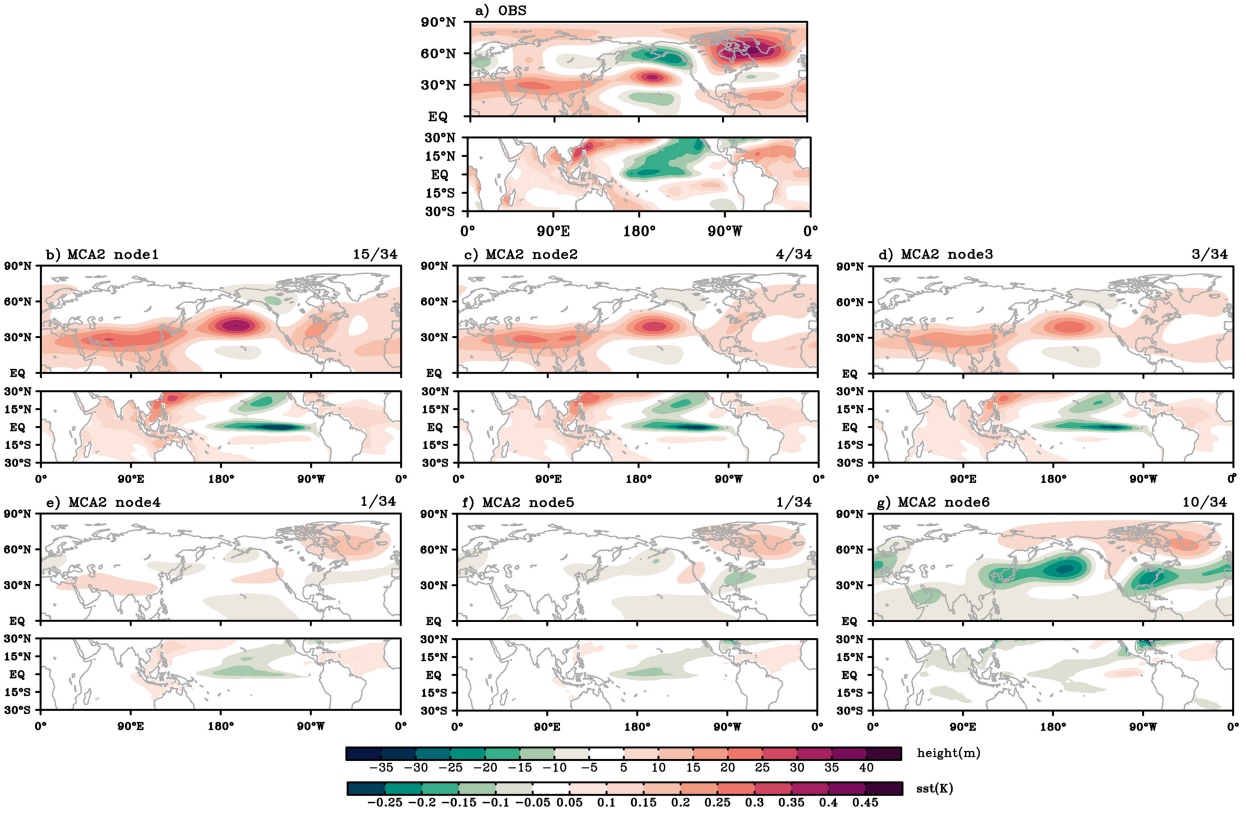

FIG. 8. Classifying simulated MCA2 by CMIP6 using the SOM method. (a) MCA2 between detrended monthly mean Z200 (m) and tropical SST (°C) in observations, and (b)–(g) 34 MCA2 from the CMIP6 models clustered into six nodes. The number of models grouped into each node is indicated in the title of each panel.

some features of the observed RWS connected to the PARC mode. This means that these high-order SST modes in the tropical Pacific in models are not strong enough in magnitude to generate sufficiently strong RWS to trigger the PARC in this region. These findings suggest that biased simulations of tropical convection and the related RWS could be a culprit responsible for models' limited capability in reproducing the PARC.

b. *Limitations in simulating summer circulation mean state over the eastern Pacific*

The other possible issue resulting in poor model simulations of the PARC teleconnection may be rooted in limitations to reproduce the NH summertime climatological mean flow especially over the eastern Pacific. Seasonal mean 200-hPa zonal winds in the multimodel ensemble means show large biases in oceanic regions, especially over the Pacific Ocean in boreal summer (Figs. 10a–d). This region serves as the key zone where the mean flow critically determines characteristics of extratropical stationary Rossby wave excitation triggered by RWS forcing associated with ENSO and high-order SST modes (Batehup et al. 2015; Hoskins and Woollings 2015). The observed zonal winds over the tropical eastern Pacific are generally westerly winds from boreal fall to spring in the upper troposphere, which is known as the westerly duct that facilitates an interaction between the tropics and extratropics and interactions of wave activities across the tropics between the two hemispheres (Webster and Holton 1982; Webster and Chang 1998). The existence of mean westerly winds over the region is more favorable for Rossby wave propagation related to ENSO-related SST variations. However, in summer, the westerly duct over this region is greatly weakened and replaced by weak easterly winds. In theory, these weak easterlies may mute the export of ENSO's influence out of the deep tropics considering that stationary Rossby waves preferentially exist and propagate in the westerly flows (Trenberth et al. 1998). Thus, the existence of subtropical westerly winds along ~20°N over the subtropical eastern Pacific in summer may optimally allow non-ENSO related SST modes to drive tropical–extratropical teleconnections like the PARC mode.

However, the simulated upper-level mean zonal flows over the tropical eastern Pacific in the multimodel ensemble means show a different structure and evolution in summer. The simulated westerly duct prevails over the region year-round, which is possibly due to an imperfect simulation of the strength of the Hadley cell or eddy-mean flow feedbacks (e.g., Webster 1961; Hartmann 2007). To better illustrate these biases, we calculate differences of seasonal mean 200-hPa zonal winds between each CMIP6 simulation and observations in the tropical eastern Pacific (0°–15°N, 80°W–180°, Fig. 10e). The negative biases mainly occur in boreal winter and spring, while positive biases are primarily seen in boreal summer and autumn. This indicates that the

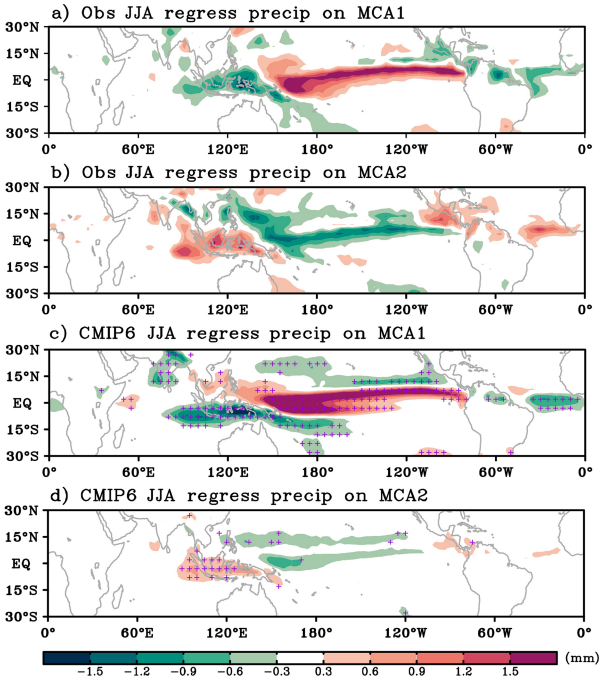

FIG. 9. Model biases in simulating observed MCA1/2 related tropical precipitation in boreal summer. The JJA GPCP precipitation regressed on the time series of (a) MCA1 and (b) MCA2 SST in observations. The regressed maps of simulated precipitation on the time series of (c) MCA1 and (d) MCA2 SST averaged from all CMIP6 models. Stippling in (c) and (d) indicates grids where a majority (more than 70%) of CMIP6 models exhibit the same sign as that of the regressed precipitation patterns in observations.

wintertime mean westerly flow tends to be underestimated in simulations, while the summertime mean easterly flow is weaker than that in observations. This type of simulated circulation mean state may still favor ENSO forcing in the summertime, unlike in the real world.

To further examine how the mean flow to the north of the source region determines poleward propagation of stationary Rossby waves, we calculate the governing stationary Rossby wavenumber [K_s; Eq. (2.3)] of the mean flow state over the entire NH to understand what types of stationary Rossby waves tend to be maintained in this area. In observations, the strong easterly basic-flow in the tropical eastern Pacific creates unfavorable conditions (K_s does not exist) along 20°–30°N that inhibits the propagation of stationary Rossby waves from the deep tropics to the subtropics (Fig. 10f). Instead, the simulated mean flow has no such barriers along 20°–30°N in the subtropics and consequently ENSO may still have a chance to suppress other teleconnections generated in the region to influence remote areas in summer (Fig. 10g). In addition, the observed K_s in the North Pacific along 30°–40°N are around 6–7 and the simulated ones are slightly smaller (~6) over most areas, indicating that the mean flow in models overall favors a stationary Rossby wave train that has a longer wavelength. This could be another reason that models have difficulty in reproducing the PARC, which has a shorter wavelength than the PNA. In summary, models' biases in simulating tropical SST and convection variability, and key properties of the mean flow in the tropical eastern Pacific may jointly make it difficult for models to successfully simulate the PARC.

6. Discussion and conclusions

In this study, we reveal two leading observed teleconnections bridging tropical SST anomalies with extratropical atmospheric circulation in the NH on interannual and interdecadal time scales. The first one manifests as the classical PNA pattern mediating the extratropical atmospheric circulation response to El Niño–type warm SST anomalies primarily in boreal winter and spring on interannual time scales. The second teleconnection, the so-called PARC mode, is more active in summer and it displays a broad range of variability from interannual to interdecadal time scales characterized by a cold Pacific–warm Arctic out-of-phase connection between the tropical SST anomalies in the eastern Pacific and Arctic climate variability. Both teleconnections have prominent impacts on surface climate conditions hemispheric wide, via differently structured Rossby wave propagation toward the high latitudes. CMIP6 models demonstrate some limitations in replicating the PARC mode but show skillful capability in simulating the midlatitude component of the PNA mode, except that the simulated PNA-driven effects over the Arctic are overestimated. The reason behind the underestimation of the PARC mode is speculated to be linked to model biases in simulating low-frequency tropical SST and associated convection and RWS variability and the atmospheric mean flow over the central and eastern Pacific in summer.

Although our assessments are carried out on the basis of historical simulations during 1979–2014, this short duration might not optimally enable us to thoroughly evaluate models' performance in capturing the PARC in a longer integration considering the possible nonstationary characteristics of the PARC on low-frequency time scales (Swart 2017; Bonan and Blanchard-Wrigglesworth 2020; Topál et al. 2020; Henderson et al. 2021). Thus, we additionally use the CESM1 Large Ensemble (CESM-LEN) 1800-yr-long control run (preindustrial simulations; Kay et al. 2015) to further investigate the model's performance in simulating the PARC and its related imprints on other fields in the tropics and extratropics. By applying MCA on the monthly mean NH Z200 and tropical SST fields in CESM-LEN long control run (1800 years), we find that the PNA mode is well captured as the leading mode but the model still struggles to replicate the PARC-like teleconnection (Fig. 11). Considering that the length of this control run is much longer than observations, we additionally divide this 1800-yr preindustrial simulation into 45 nonoverlapping segments (each with a 40-yr-long duration) and examine the representation of the PARC in each segment. It is encouraging that a few segments out of the 45 segments (around 10%) are able to capture some observed features of the PARC (figures not shown). In all these "good segments" the tropical cold SST over eastern Pacific is well reflected, suggesting that the model has some potential to simulate the PARC, although the necessary conditions contributing to this success over some periods remain unclear. The results remain the same even with a larger sample size of overlapping segments (each still with a 40-yr-long

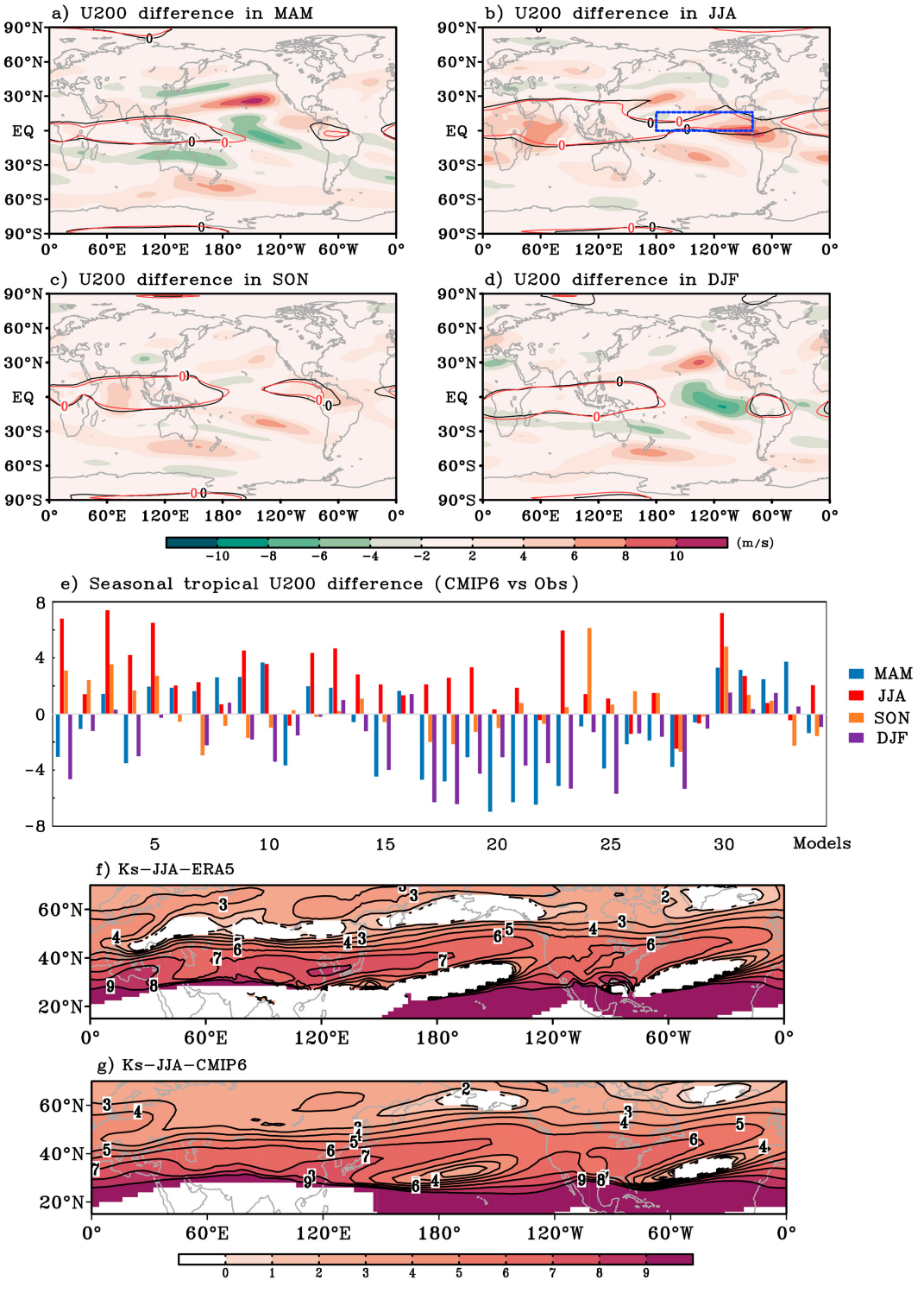

FIG. 10. Model biases in simulating climatological (1979–2014) seasonal mean 200-hPa zonal winds in ERA5. The difference of climatological seasonal mean 200-hPa zonal winds (m s^{-1}) between the multimodel ensemble means and ERA5 (model minus ERA5) in (a) MAM, (b) JJA, (c) SON, and (d) DJF. (e) The differences of climatological seasonal means of 200-hPa zonal winds over the tropical eastern Pacific [the blue box in (b); 0°–16°N, 80°W–180°] between each model and ERA5 in each season (model minus ERA5). The stationary Rossby wavenumbers [K_s; Eq. (2.3)] based on JJA mean 200-hPa zonal flows in (f) ERA5 and (g) the multimodel ensemble means. In (a)–(d), the contours are climatological seasonal mean 200-hPa zonal winds that are equal to zero (the black contours for observations and the red contours for the multimodel ensemble means).

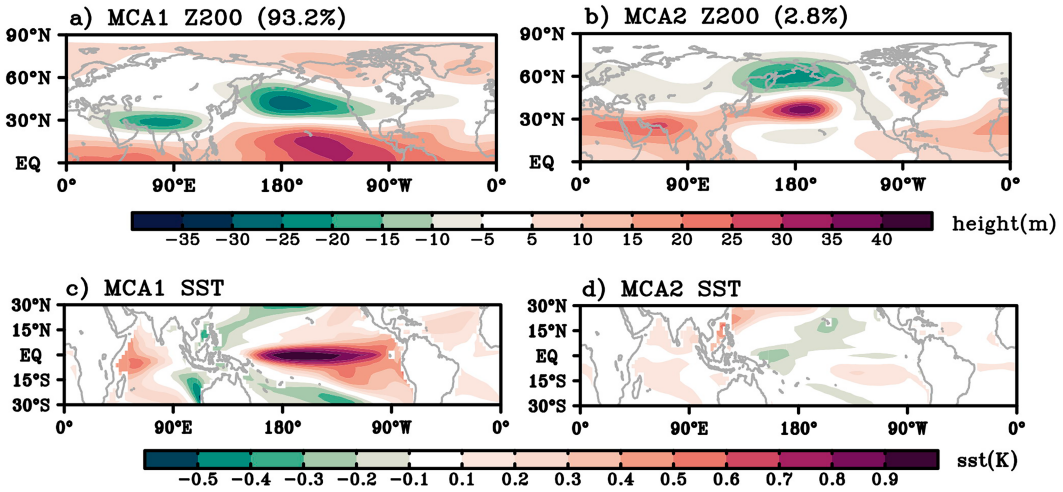

FIG. 11. The two leading NH teleconnection modes simulated in the CESM-LEN 1800-yr preindustrial simulation. MCA1 between monthly (a) Z200 (m) and (c) tropical SST (°C) in the 1800-yr-long preindustrial run. (b),(d) As in (a) and (c), but for MCA2. The SCF explained by each MCA mode is indicated in the title of each panel in (a) and (b).

duration) in CESM-LEN long control run. The probability density function (PDF) of the spatial correlations between MCA2 derived separately from these segments and the observed counterpart shows that the odds that the model (over any consecutive 40-yr period) can well capture observed MCA2 (the spatial correlation > 0.7) are about 10%–20% (supplemental Fig. 3). It is interesting to note that those "good segments" generally capture cold SST anomalies extending from the tropical central Pacific to the Gulf of California (supplemental Fig. 4). This indicates that the tilted cold SST pattern may play a role in shaping the PARC mode in the NH extratropics. Furthermore, we cannot rule out the possibility that the appearance of the PARC in the recent 40-yr reanalysis may also partially originate from internal variability of the climate system and its recent strengthening may be time dependent. Additionally, the spatial structure of the PARC mode as identified by the MCA analysis of two reanalysis datasets (Figs. 1 and 4) also exhibits slight variations across different time periods, indicating the need for further understanding the PARC's sensitivity to tropical SST forcing over the past 110 years.

Since a poor simulation of low-frequency tropical SST variability is speculated as one cause of models' biases in capturing the PARC, it is worth examining whether the PARC mode is well replicated in the Atmospheric Model Intercomparison Project (AMIP)-type or Pacific pacemaker runs in which tropical SST is constrained by observed variability. Here we mainly evaluate the performance of the 10-member Tropical Ocean Global Atmosphere (TOGA forced by ERSST5) and 20-member Pacific pacemaker ensembles (Deser et al. 2017a,b) developed by the Climate Variability and Change Working Group (CVCWG) using CESM1. By applying the same MCA method on the monthly mean NH Z200 and tropical SST fields in these runs, we find that the performance in reproducing the PNA and PARC is the same as those CMIP-type runs without specifying observed SST in the tropics (figures not shown). One possibility that the performance is not significantly improved in these AMIP-type runs is that observed rainfall changes in the tropical Pacific result from active atmosphere–ocean coupling rather than a one-way response of the atmosphere to SST forcing as designed in AMIP runs (Wang et al. 2005). Thus, although observed tropical SST variability is well specified in these runs, the rainfall variability and associated diabatic forcing that drive large-scale teleconnections may not be correctly simulated.

Based on our analysis and many others, it is inspiring that most models can successfully capture the PNA mode, suggesting a high potential to achieve skillful seasonal predictions in winter associated with ENSO's variability (Yeh et al. 2018; McCrystall and Screen 2021). However, one concern is that simulated ENSO variability in some of these climate models could be overestimated (L'Heureux et al. 2017), especially in the high latitudes, which may reduce the diversity of teleconnections that should operate in models and thus overwhelm other types of teleconnections with temporal characteristics on lower frequency time scales (such as the PARC). Thus, a lack of reasonable representations of the PARC in most climate models is likely to have far-reaching and unanticipated consequences on decadal prediction and climate projection of high-latitude climate variability, especially over the Arctic (Hanna et al. 2016; Meehl et al. 2018; Hall et al. 2021).

Progress on decadal predictions has developed rapidly over the past decades, raising awareness of the still insufficient skill of current models in predicting climate over land areas in the middle and high latitudes and some parts of oceans (Meehl et al. 2009, 2014; Liu 2012; Sigmond and Fyfe 2016). The PARC mode contributes to a substantial portion of high-latitude land climate variability in the recent decades over Eurasia and North America. Thus, the better representation of low-frequency SST variability and the mean state over the eastern Pacific and atmospheric responses to low-frequency SST variability in the form of the PARC may lead to a breakthrough of improved decadal prediction of mid- and high-latitude climate. In addition, what is

noteworthy is why external forcing prefers to project on the PARC mode in recent decades and whether this mode is linked with aerosol-driven forcing, which need to be investigated further in future studies.

In summary, the reasons leading to the limitation of most CMIP6 models in capturing the PARC are complex and manifold. One possibility is that the PARC may own some internal origins and tropical SST serves as an important trigger. Without tropical SST forcing, it can also be generated by other mechanisms, such as instability of the mean state or external radiative forcing. A second possibility may be that current models lack capabilities to represent some essential components of PARC's linkage from tropical forcing to the extratropical circulation response. Given diverse performances of current models in simulating the PARC, our study is meant to highlight both the possibilities and the priority of needed next steps to improve climate model skill in comprehensively replicating observed NH tropical–extratropical teleconnections, including both the PNA and PARC. Since this study primarily focuses on tropical–extratropical teleconnections on a hemispheric scale that appeared to be dominated by tropical Pacific SST modes, it should be noted that tropical SST over other basins may be also important to drive regional extratropical teleconnections (Sigmond and Fyfe 2016; Dunn-Sigouin et al. 2021; Henderson et al. 2021) that cannot be successfully captured by our MCA method. Future analyses emphasizing these regional teleconnections originating from other tropical basins may be necessary to enrich our understanding of tropical–extratropical teleconnections in the NH.

Acknowledgments. This study was supported by the Modeling, Analysis, Predictions and Projections (NA19OAR4310281) and Climate Variability and Predictability (NA18OAR4310424) programs as part of NOAA's Climate Program Office. X. F. was jointly supported by China Scholarship Council (CSC) scholarship (201808320280), Shanghai Post-Doctoral Excellence Program (2021021), NA18OAR4310424 and the National Natural Science Foundation of China (41730961). Q. D. was supported by NSF OPP 2246601 and CVP NA23OAR4310273. L. W. was supported by the National Natural Science Foundation of China (41730961). D. T. was supported by the ÚNKP-21-3 New National Excellence Program of the Ministry for Innovation and Technology and 2019-2.1.11-TÉT-2020-00114 from the source of the National Research, Development and Innovation fund. We acknowledge the CESM Large Ensemble Community Project and U.S. CLIVAR Large Ensemble Working Group.

Data availability statement. ERA5 and ERA-20C century-long reanalysis datasets are available from https://www.ecmwf.int/. Global SST data from the NOAA extended reconstructed SST version 5 (ERSSTv5), sea ice extent data from the National Snow and Ice Data Center (NSIDC) and precipitation data from the Global Precipitation Climatology Project (GPCP) are obtained from https://www.ncei.noaa.gov/products/extended-reconstructed-sst, https://nsidc.org/data, and https://psl.noaa.gov/data/gridded/data.gpcp.html, respectively. The CMIP6 simulations employed in this study are available from the Earth System Grid Federation from https://esgf-node.llnl.gov/search/cmip6/. The CESM-LEN 1800-yr-long control runs and the observed-SST-forced CESM1 simulations (1880–2017) are provided by the Climate Variability and Change Working Group (CVCWG), which is available from https://www.cesm.ucar.edu/working_groups/CVC/. The SOM package used in this study is developed by MATLAB. The maximum covariance analysis (MCA) code is available on request from the corresponding author.

REFERENCES

Adler, R. F., and Coauthors, 2003: The version 2 Global Precipitation Climatology Project (GPCP) monthly precipitation analysis (1979–present). *J. Hydrometeor.*, **4**, 1147–1167, https://doi.org/10.1175/1525-7541(2003)004<1147:TVGPCP>2.0.CO;2.

Baggett, C., and S. Lee, 2015: Arctic warming induced by tropically forced tapping of available potential energy and the role of the planetary-scale waves. *J. Atmos. Sci.*, **72**, 1562–1568, https://doi.org/10.1175/JAS-D-14-0334.1.

Barnston, A. G., and R. E. Livezey, 1987: Classification, seasonality and persistence of low-frequency atmospheric circulation patterns. *Mon. Wea. Rev.*, **115**, 1083–1126, https://doi.org/10.1175/1520-0493(1987)115<1083:CSAPOL>2.0.CO;2.

Batehup, R., S. McGregor, and A. J. E. Gallant, 2015: The influence of non-stationary teleconnections on palaeoclimate reconstructions of ENSO variance using a pseudoproxy framework. *Climate Past*, **11**, 1733–1749, https://doi.org/10.5194/cp-11-1733-2015.

Baxter, I., and Coauthors, 2019: How tropical Pacific surface cooling contributed to accelerated sea ice melt from 2007 to 2012 as ice is thinned by anthropogenic forcing. *J. Climate*, **32**, 8583–8602, https://doi.org/10.1175/JCLI-D-18-0783.1.

Bonan, D. B., and E. Blanchard-Wrigglesworth, 2020: Nonstationary teleconnection between the Pacific Ocean and Arctic sea ice. *Geophys. Res. Lett.*, **47**, e2019GL085666, https://doi.org/10.1029/2019GL085666.

Bretherton, C. S., C. Smith, and J. M. Wallace, 1992: An intercomparison of methods for finding coupled patterns in climate data. *J. Climate*, **5**, 541–560, https://doi.org/10.1175/1520-0442(1992)005<0541:AIOMFF>2.0.CO;2.

——, M. Widmann, V. P. Dymnikov, J. M. Wallace, and I. Bladé, 1999: The effective number of spatial degrees of freedom of a time-varying field. *J. Climate*, **12**, 1990–2009, https://doi.org/10.1175/1520-0442(1999)012<1990:TENOSD>2.0.CO;2.

Cavalieri, D. J., C. L. Parkinson, P. Gloersen, and H. J. Zwally, 1996: Sea ice concentrations from Nimbus-7 SMMR and DMSP SSM/I-SSMIS passive microwave data, version 1. NASA National Snow and Ice Data Center Distributed Active Archive Center, accessed 7 December 2023, https://doi.org/10.5067/8GQ8LZQVL0VL.

Chen, Z., B. Gan, L. Wu, and F. Jia, 2018: Pacific–North American teleconnection and North Pacific Oscillation: Historical simulation and future projection in CMIP5 models. *Climate Dyn.*, **50**, 4379–4403, https://doi.org/10.1007/s00382-017-3881-9.

Chiang, J. C. H., and D. J. Vimont, 2004: Analogous Pacific and Atlantic meridional modes of tropical atmosphere–ocean variability. *J. Climate*, **17**, 4143–4158, https://doi.org/10.1175/JCLI4953.1.

Choi, K.-S., C.-C. Wu, and E.-J. Cha, 2010: Change of tropical cyclone activity by Pacific-Japan teleconnection pattern in the western North Pacific. *J. Geophys. Res.*, **115**, D19114, https://doi.org/10.1029/2010JD013866.

Cohen, J., 2016: An observational analysis: Tropical relative to Arctic influence on midlatitude weather in the era of Arctic

amplification. *Geophys. Res. Lett.*, **43**, 5287–5294, https://doi.org/10.1002/2016GL069102.

Deser, C., A. Phillips, V. Bourdette, and H. Teng, 2012a: Uncertainty in climate change projections: The role of internal variability. *Climate Dyn.*, **38**, 527–546, https://doi.org/10.1007/s00382-010-0977-x.

——, and Coauthors, 2012b: ENSO and Pacific decadal variability in the Community Climate System Model version 4. *J. Climate*, **25**, 2622–2651, https://doi.org/10.1175/JCLI-D-11-00301.1.

——, R. Guo, and F. Lehner, 2017a: The relative contributions of tropical Pacific sea surface temperatures and atmospheric internal variability to the recent global warming hiatus. *Geophys. Res. Lett.*, **44**, 7945–7954, https://doi.org/10.1002/2017GL074273.

——, I. R. Simpson, K. A. McKinnon, and A. S. Phillips, 2017b: The Northern Hemisphere extratropical atmospheric circulation response to ENSO: How well do we know it and how do we evaluate models accordingly? *J. Climate*, **30**, 5059–5082, https://doi.org/10.1175/JCLI-D-16-0844.1.

Ding, Q., and B. Wang, 2005: Circumglobal teleconnection in the Northern Hemisphere summer. *J. Climate*, **18**, 3483–3505, https://doi.org/10.1175/JCLI3473.1.

——, E. J. Steig, D. S. Battisti, and M. Küttel, 2011: Winter warming in West Antarctica caused by central tropical Pacific warming. *Nat. Geosci.*, **4**, 398–403, https://doi.org/10.1038/ngeo1129.

——, J. M. Wallace, D. S. Battisti, E. J. Steig, A. J. E. Gallant, H. J. Kim, and L. Geng, 2014: Tropical forcing of the recent rapid Arctic warming in northeastern Canada and Greenland. *Nature*, **509**, 209–212, https://doi.org/10.1038/nature13260.

Dunn-Sigouin, E., C. Li, and P. J. Kushner, 2021: Limited influence of localized tropical sea-surface temperatures on moisture transport into the Arctic. *Geophys. Res. Lett.*, **48**, e2020GL091540, https://doi.org/10.1029/2020GL091540.

Eyring, V., S. Bony, G. A. Meehl, C. A. Senior, B. Stevens, R. J. Stouffer, and K. E. Taylor, 2016: Overview of the Coupled Model Intercomparison Project phase 6 (CMIP6) experimental design and organization. *Geosci. Model Dev.*, **9**, 1937–1958, https://doi.org/10.5194/gmd-9-1937-2016.

Fasullo, J. T., A. S. Phillips, and C. Deser, 2020: Evaluation of leading modes of climate variability in the CMIP archives. *J. Climate*, **33**, 5527–5545, https://doi.org/10.1175/JCLI-D-19-1024.1.

Feng, X., and Coauthors, 2021: A multidecadal-scale tropically driven global teleconnection over the past millennium and its recent strengthening. *J. Climate*, **34**, 2549–2565, https://doi.org/10.1175/JCLI-D-20-0216.1.

Fetterer, F., and K. Knowles, 2004: Sea ice index monitors polar ice extent. *Eos, Trans. Amer. Geophys. Union*, **85**, 163, https://doi.org/10.1029/2004EO160007.

Gibson, P. B., S. E. Perkins-Kirkpatrick, P. Uotila, A. S. Pepler, and L. V. Alexander, 2017: On the use of self-organizing maps for studying climate extremes. *J. Geophys. Res. Atmos.*, **122**, 3891–3903, https://doi.org/10.1002/2016JD026256.

Hall, R. J., E. Hanna, and L. Chen, 2021: Winter Arctic amplification at the synoptic timescale, 1979–2018, its regional variation and response to tropical and extratropical variability. *Climate Dyn.*, **56**, 457–473, https://doi.org/10.1007/s00382-020-05485-y.

Hanna, E., T. E. Cropper, R. J. Hall, and J. Cappelen, 2016: Greenland blocking index 1851–2015: A regional climate change signal. *Int. J. Climatol.*, **36**, 4847–4861, https://doi.org/10.1002/joc.4673.

Hartmann, D. L., 2007: The atmospheric general circulation and its variability. *J. Meteor. Soc. Japan*, **85B**, 123–143, https://doi.org/10.2151/jmsj.85B.123.

Henderson, G. R., B. S. Barrett, L. J. Wachowicz, K. S. Mattingly, J. R. Preece, and T. L. Mote, 2021: Local and remote atmospheric circulation drivers of Arctic change: A review. *Front. Earth Sci.*, **9**, 709896, https://doi.org/10.3389/feart.2021.709896.

Herbst, M., H. V. Gupta, and M. C. Casper, 2009: Mapping model behaviour using self-organizing maps. *Hydrol. Earth Syst. Sci.*, **13**, 395–409, https://doi.org/10.5194/hess-13-395-2009.

Hersbach, H., and Coauthors, 2020: The ERA5 global reanalysis. *Quart. J. Roy. Meteor. Soc.*, **146**, 1999–2049, https://doi.org/10.1002/qj.3803.

Horel, J. D., and J. M. Wallace, 1981: Planetary-scale atmospheric phenomena associated with the Southern Oscillation. *Mon. Wea. Rev.*, **109**, 813–829, https://doi.org/10.1175/1520-0493(1981)109<0813:PSAPAW>2.0.CO;2.

Hoskins, B. J., and T. Ambrizzi, 1993: Rossby wave propagation on a realistic longitudinally varying flow. *J. Atmos. Sci.*, **50**, 1661–1671, https://doi.org/10.1175/1520-0469(1993)050<1661:RWPOAR>2.0.CO;2.

——, and T. Woollings, 2015: Persistent extratropical regimes and climate extremes. *Curr. Climate Change Rep.*, **1**, 115–124, https://doi.org/10.1007/s40641-015-0020-8.

Hu, C., S. Yang, Q. Wu, Z. Li, J. Chen, K. Deng, T. Zhang, and C. Zhang, 2016: Shifting El Niño inhibits summer Arctic warming and Arctic sea-ice melting over the Canada Basin. *Nat. Commun.*, **7**, 11721, https://doi.org/10.1038/ncomms11721.

Huang, B., and Coauthors, 2017: Extended reconstructed sea surface temperature, version 5 (ERSSTv5): Upgrades, validations, and intercomparisons. *J. Climate*, **30**, 8179–8205, https://doi.org/10.1175/JCLI-D-16-0836.1.

Jeong, H., H.-S. Park, M. F. Stuecker, and S.-W. Yeh, 2022: Record low Arctic sea ice extent in 2012 linked to two-year La Niña-driven sea surface temperature pattern. *Geophys. Res. Lett.*, **49**, e2022GL098385, https://doi.org/10.1029/2022GL098385.

Joseph, P. V., and J. Srinivasan, 1999: Rossby waves in May and the Indian summer monsoon rainfall. *Tellus*, **51A**, 854–864, https://doi.org/10.3402/tellusa.v51i5.14497.

Karnauskas, K. B., J. E. Smerdon, R. Seager, and J. F. González-Rouco, 2012: A Pacific centennial oscillation predicted by coupled GCMs. *J. Climate*, **25**, 5943–5961, https://doi.org/10.1175/JCLI-D-11-00421.1.

Kay, J. E., and Coauthors, 2015: The Community Earth System Model (CESM) large ensemble project: A community resource for studying climate change in the presence of internal climate variability. *Bull. Amer. Meteor. Soc.*, **96**, 1333–1349, https://doi.org/10.1175/BAMS-D-13-00255.1.

Kohonen, T., 1990: The self-organizing map. *Proc. IEEE*, **78**, 1464–1480, https://doi.org/10.1109/5.58325.

Kosaka, Y., and H. Nakamura, 2010: Mechanisms of meridional teleconnection observed between a summer monsoon system and a subtropical anticyclone. Part I: The Pacific–Japan pattern. *J. Climate*, **23**, 5085–5108, https://doi.org/10.1175/2010JCLI3413.1.

——, ——, M. Watanabe, and M. Kimoto, 2009: Analysis on the dynamics of a wave-like teleconnection pattern along the summertime Asian jet based on a reanalysis dataset and climate model simulations. *J. Meteor. Soc. Japan*, **87**, 561–580, https://doi.org/10.2151/jmsj.87.561.

Larson, S. M., D. J. Vimont, A. C. Clement, and B. P. Kirtman, 2018: How momentum coupling affects SST variance and large-scale Pacific climate variability in CESM. *J. Climate*, **31**, 2927–2944, https://doi.org/10.1175/JCLI-D-17-0645.1.

Lewis, S. C., and A. N. LeGrande, 2015: Stability of ENSO and its tropical Pacific teleconnections over the last millennium. *Climate Past*, **11**, 1347–1360, https://doi.org/10.5194/cp-11-1347-2015.

L'Heureux, M. L., M. K. Tippett, A. Kumar, A. H. Butler, L. M. Ciasto, Q. Ding, K. J. Harnos, and N. C. Johnson, 2017: Strong relations between ENSO and the Arctic Oscillation in the North American Multimodel Ensemble. *Geophys. Res. Lett.*, **44**, 11 654–11 662, https://doi.org/10.1002/2017GL074854.

Lin, H., G. Brunet, and J. Derome, 2009: An observed connection between the North Atlantic Oscillation and the Madden–Julian oscillation. *J. Climate*, **22**, 364–380, https://doi.org/10.1175/2008JCLI2515.1.

Liu, Z., 2012: Dynamics of interdecadal climate variability: A historical perspective. *J. Climate*, **25**, 1963–1995, https://doi.org/10.1175/2011JCLI3980.1.

——, Y. Tang, Z. Jian, C. J. Poulsen, J. M. Welker, and G. J. Bowen, 2017: Pacific North American circulation pattern links external forcing and North American hydroclimatic change over the past millennium. *Proc. Natl. Acad. Sci. USA*, **114**, 3340–3345, https://doi.org/10.1073/pnas.1618201114.

Lu, R.-Y., J.-H. Oh, and B.-J. Kim, 2002: A teleconnection pattern in upper-level meridional wind over the North African and Eurasian continent in summer. *Tellus*, **54A**, 44–55, https://doi.org/10.3402/tellusa.v54i1.12122.

Matsumura, S., and Y. Kosaka, 2019: Arctic-Eurasian climate linkage induced by tropical ocean variability. *Nat. Commun.*, **10**, 3441, https://doi.org/10.1038/s41467-019-11359-7.

McCrystall, M. R., and J. A. Screen, 2021: Arctic winter temperature variations correlated with ENSO are dependent on coincidental sea ice changes. *Geophys. Res. Lett.*, **48**, e2020GL091519, https://doi.org/10.1029/2020GL091519.

——, J. S. Hosking, I. P. White, and A. C. Maycock, 2020: The impact of changes in tropical sea surface temperatures over 1979–2012 on Northern Hemisphere high-latitude climate. *J. Climate*, **33**, 5103–5121, https://doi.org/10.1175/JCLI-D-19-0456.1.

Meehl, G. A., and Coauthors, 2009: Decadal prediction. *Bull. Amer. Meteor. Soc.*, **90**, 1467–1486, https://doi.org/10.1175/2009BAMS2778.1.

——, and Coauthors, 2014: Decadal climate prediction: An update from the trenches. *Bull. Amer. Meteor. Soc.*, **95**, 243–267, https://doi.org/10.1175/BAMS-D-12-00241.1.

——, C. T. Y. Chung, J. M. Arblaster, M. M. Holland, and C. M. Bitz, 2018: Tropical decadal variability and the rate of Arctic sea ice decrease. *Geophys. Res. Lett.*, **45**, 11 326–11 333, https://doi.org/10.1029/2018GL079989.

Mori, M., M. Watanabe, H. Shiogama, J. Inoue, and M. Kimoto, 2014: Robust Arctic sea-ice influence on the frequent Eurasian cold winters in past decades. *Nat. Geosci.*, **7**, 869–873, https://doi.org/10.1038/ngeo2277.

Neelin, J. D., and Coauthors, 1992: Tropical air-sea interaction in general circulation models. *Climate Dyn.*, **7**, 73–104, https://doi.org/10.1007/BF00209610.

Orbe, C., and Coauthors, 2020: Representation of modes of variability in six U.S. climate models. *J. Climate*, **33**, 7591–7617, https://doi.org/10.1175/JCLI-D-19-0956.1.

Perlwitz, J., M. Hoerling, and R. Dole, 2015: Arctic tropospheric warming: Causes and linkages to lower latitudes. *J. Climate*, **28**, 2154–2167, https://doi.org/10.1175/JCLI-D-14-00095.1.

Plumb, R. A., 1985: On the three-dimensional propagation of stationary waves. *J. Atmos. Sci.*, **42**, 217–229, https://doi.org/10.1175/1520-0469(1985)042<0217:OTTDPO>2.0.CO;2.

Reusser, D. E., T. Blume, B. Schaefli, and E. Zehe, 2009: Analysing the temporal dynamics of model performance for hydrological models. *Hydrol. Earth Syst. Sci.*, **13**, 999–1018, https://doi.org/10.5194/hess-13-999-2009.

Sardeshmukh, P. D., and B. J. Hoskins, 1988: The generation of global rotational flow by steady idealized tropical divergence. *J. Atmos. Sci.*, **45**, 1228–1251, https://doi.org/10.1175/1520-0469(1988)045<1228:TGOGRF>2.0.CO;2.

Seo, K.-H., and S.-W. Son, 2012: The global atmospheric circulation response to tropical diabatic heating associated with the Madden–Julian oscillation during northern winter. *J. Atmos. Sci.*, **69**, 79–96, https://doi.org/10.1175/2011JAS3686.1.

Shen, Z., Y. Ming, and I. M. Held, 2020: Using the fast impact of anthropogenic aerosols on regional land temperature to constrain aerosol forcing. *Sci. Adv.*, **6**, eabb5297, https://doi.org/10.1126/sciadv.abb5297.

Sigmond, M., and J. C. Fyfe, 2016: Tropical Pacific impacts on cooling North American winters. *Nat. Climate Change*, **6**, 970–974, https://doi.org/10.1038/nclimate3069.

Stan, C., D. M. Straus, J. S. Frederiksen, H. Lin, E. D. Maloney, and C. Schumacher, 2017: Review of tropical-extratropical teleconnections on intraseasonal time scales. *Rev. Geophys.*, **55**, 902–937, https://doi.org/10.1002/2016RG000538.

Stickler, A., and Coauthors, 2014: ERA-CLIM: Historical surface and upper-air data for future reanalyses. *Bull. Amer. Meteor. Soc.*, **95**, 1419–1430, https://doi.org/10.1175/BAMS-D-13-00147.1.

Stoner, A. M. K., K. Hayhoe, and D. J. Wuebbles, 2009: Assessing general circulation model simulations of atmospheric teleconnection patterns. *J. Climate*, **22**, 4348–4372, https://doi.org/10.1175/2009JCLI2577.1.

Sun, D.-Z., T. Zhang, Y. Sun, and Y. Yu, 2014: Rectification of El Niño–Southern Oscillation into climate anomalies of decadal and longer time scales: Results from forced ocean GCM experiments. *J. Climate*, **27**, 2545–2561, https://doi.org/10.1175/JCLI-D-13-00390.1.

Swart, N., 2017: Natural causes of Arctic sea-ice loss. *Nat. Climate Change*, **7**, 239–241, https://doi.org/10.1038/nclimate3254.

Topál, D., Q. Ding, J. Mitchell, I. Baxter, M. Herein, T. Haszpra, R. Luo, and Q. Li, 2020: An internal atmospheric process determining summertime Arctic sea ice melting in the next three decades: Lessons learned from five large ensembles and multiple CMIP5 climate simulations. *J. Climate*, **33**, 7431–7454, https://doi.org/10.1175/JCLI-D-19-0803.1.

Trenberth, K. E., G. W. Branstator, D. Karoly, A. Kumar, N.-C. Lau, and C. Ropelewski, 1998: Progress during TOGA in understanding and modeling global teleconnections associated with tropical sea surface temperatures. *J. Geophys. Res.*, **103**, 14 291–14 324, https://doi.org/10.1029/97JC01444.

——, J. T. Fasullo, G. Branstator, and A. S. Phillips, 2014: Seasonal aspects of the recent pause in surface warming. *Nat. Climate Change*, **4**, 911–916, https://doi.org/10.1038/nclimate2341.

Vavrus, S. J., 2018: The influence of Arctic amplification on mid-latitude weather and climate. *Curr. Climate Change Rep.*, **4**, 238–249, https://doi.org/10.1007/s40641-018-0105-2.

Wakabayashi, S., and R. Kawamura, 2004: Extraction of major teleconnection patterns possibly associated with the anomalous summer climate in Japan. *J. Meteor. Soc. Japan*, **82**, 1577–1588, https://doi.org/10.2151/jmsj.82.1577.

Wallace, J. M., and D. S. Gutzler, 1981: Teleconnections in the geopotential height field during the Northern Hemisphere winter. *Mon. Wea. Rev.*, **109**, 784–812, https://doi.org/10.1175/1520-0493(1981)109<0784:TITGHF>2.0.CO;2.

——, C. Smith, and C. S. Bretherton, 1992: Singular value decomposition of wintertime sea surface temperature and 500-mb height

anomalies. *J. Climate*, **5**, 561–576, https://doi.org/10.1175/1520-0442(1992)005<0561:SVDOWS>2.0.CO;2.

Wang, B., R. Wu, and X. Fu, 2000: Pacific–East Asian teleconnection: How does ENSO affect East Asian climate? *J. Climate*, **13**, 1517–1536, https://doi.org/10.1175/1520-0442(2000)013<1517:PEATHD>2.0.CO;2.

——, Q. Ding, X. Fu, I.-S. Kang, K. Jin, J. Shukla, and F. Doblas-Reyes, 2005: Fundamental challenge in simulation and prediction of summer monsoon rainfall. *Geophys. Res. Lett.*, **32**, L15711, https://doi.org/10.1029/2005GL022734.

Wang, L., P. Xu, W. Chen, and Y. Liu, 2017: Interdecadal variations of the Silk Road pattern. *J. Climate*, **30**, 9915–9932, https://doi.org/10.1175/JCLI-D-17-0340.1.

Webster, F., 1961: The effect of meanders on the kinetic energy balance of the Gulf Stream. *Tellus*, **13**, 392–401, https://doi.org/10.3402/tellusa.v13i3.9515.

Webster, P. J., and J. R. Holton, 1982: Cross-equatorial response to middle-latitude forcing in a zonally varying basic state. *J. Atmos. Sci.*, **39**, 722–733, https://doi.org/10.1175/1520-0469(1982)039<0722:CERTML>2.0.CO;2.

——, and H.-R. Chang, 1998: Atmospheric wave propagation in heterogeneous flow: Basic flow controls on tropical-extratropical interaction and equatorial wave modification. *Dyn. Atmos. Oceans*, **27**, 91–134, https://doi.org/10.1016/S0377-0265(97)00003-1.

Wu, B., T. Zhou, C. Li, W. A. Müller, and J. Lin, 2019: Improved decadal prediction of Northern-Hemisphere summer land temperature. *Climate Dyn.*, **53**, 1357–1369, https://doi.org/10.1007/s00382-019-04658-8.

Yeh, S.-W., and Coauthors, 2018: ENSO atmospheric teleconnections and their response to greenhouse gas forcing. *Rev. Geophys.*, **56**, 185–206, https://doi.org/10.1002/2017RG000568.

Yuan, X., M. R. Kaplan, and M. A. Cane, 2018: The interconnected global climate system—A review of tropical–polar teleconnections. *J. Climate*, **31**, 5765–5792, https://doi.org/10.1175/JCLI-D-16-0637.1.